2. Physical Properties of Solids

Results from new directions in research programs designed to accommodate the expanded goals of ERDA and Oak Ridge National Laboratory in nonnuclear energy research have been encouraging during the past year. Extensive research into the behavior of ceramic oxides under hostile conditions is reported here, and the new emphasis on examination of fluxoid properties in type-II superconductors has continued. The dynamic nature of our research effort is also shown by reports of work in two areas new to the Division, fast ion conduction and fracture; the former is supported by funds from the ORNL Exploratory Studies Program. Cooperative research efforts between groups within the Division and with groups in other ORNL Divisions or at other laboratories have continued to be a source of research strength. The extent of these cooperative efforts is indicated by the many reports herein with coauthors from outside the Division.

Research on trapped-hole defects in the alkaline-earth oxides has continued. Studies focused primarily on light-element impurities (hydrogen, deuterium, and lithium) and their effect on defects and defect-controlled processes. Magnetic resonance studies of the hydrogen and deuterium defects revealed that the relaxation of the SrO lattice about the defect has a pronounced isotopic dependence. This gives a unique insight into the dynamical nature of the interaction between the defect and lattice. A new phenomenon involving radiation-induced diffusion of hydrogen and deuterium in MgO was discovered. Substitutional hydrogen and deuterium are not mobile in MgO below 800 K, but they diffuse rapidly during exposure to ionizing radiation even at much lower temperatures. A significant reduction of radiation damage due to reactor neutrons was attained by doping MgO with lithium. The usefulness of MgO as a ceramic in high-radiation fields is consequently enhanced. In addition, it was discovered that thermal quenching of lithium-doped MgO from high temperatures creates holes that are bound to substitutional Li^+ ions with high thermal stability; this contradicts the previously held concepts of the production and stability of the entire class of trapped-hole defects in the oxides. The high thermal stability of the $[Li]^0$ defects in quenched crystals was exploited in optical dichroism studies that have given new information on the electronic structure of the defects. These results aid in an evaluation of the existing theoretical models of the trapped-hole centers, and they have useful implications for current theoretical calculations at ORNL. The complex effects of high temperatures and electric fields on the electrical and mechanical properties of MgO continue to be studied. Conditions leading to and methods for avoiding catastrophic failure have been defined. Also, a better understanding has been gained of the roles that extended defects and transition metal impurities play in the conduction process.

The superconductivity research program has concentrated on gaining an understanding of the properties of fluxoids in type-II superconductors. Three separate but related problems are under investigation: anisotropy of the equilibrium properties of the fluxoid lattice in single crystal samples, fluxoid motion, and fluxoid-pinning

interactions. Anisotropy studies have been carried out using bulk magnetization and neutron diffraction techniques. Results of the latter studies are described in another section of this report. Equilibrium properties are of interest from a fundamental point of view, but they are also essential for interpreting data concerning fluxoid motion and pinning. Altering the defect structure in a controlled way by irradiation has aided the investigations of fluxoid pinning. While a few simple models describe fluxoid motion in certain experimental situations, a complete understanding has not been reached because of the complexity of the motion. Recent focus has been on work in areas in which simple models, such as the critical-state model, fail. Some effort also has been devoted to evaluating the superconducting properties of new or exotic materials as they become available.

The surface properties program is currently emphasing research in four areas: (1) Auger electron spectrometry, (2) investigations of materials in which the interplanar spacing of the surface layer differs from that of the bulk, (3) studies of clean materials which reorder such that the surface layer is out of registry with the bulk, and (4) the effects of adsorption of simple species on the previous processes. Auger spectrometry has focused on the angular dependence of electron emission and upon line-shape analysis of the angular integrated Auger signal. The first low energy electron diffraction (LEED) analysis performed at ORNL has shown that the Cu (1 10) surface is contracted with respect to that of the bulk, and the use of the combined techniques of LEED and positive ion-channeling spectroscopy to examine reordered surfaces has continued.

Studies of photovoltaic conversion of solar energy continue to be directed toward fully exploring the advantages and disadvantages of neutron-transmutation-doped (NTD) silicon in solar cell research and development. Silicon is a particularly attractive candidate for transmutation doping because it has only one isotope which transmutes to a new element, that is, phosphorus, a standard *n*-type dopant in silicon. The rate of introduction of phosphorus into silicon by the transmutation process is such that doping concentrations of interest to the semiconductor industry are readily attainable in many reactors. Neutron-transmutation-doped silicon provides four clearly identifiable advantages over silicon doped by more traditional chemical techniques. These are (1) areal and spatial uniformity of dopant distribution, (2) precise control of doping level, (3) elimination of dopant segregation at grain boundaries in polycrystalline silicon, and (4) superior control of heavy-atom contaminants. Uniformity of doping has proved to be of importance in a number of device applications, particularly high-power rectifiers and thyristors. The precise control of doping levels provides a method for very accurately compensating material to be used in radiation detectors. Neutron-transmutation-doped silicon has the disadvantage that the lattice damage introduced by the neutron irradiation must be annealed before the desired electrical properties can be recovered. Much of the photovoltaic work discussed in this report has had the objective of determining the characteristics of the lattice damage in NTD silicon and the time and temperature schedules for its annealing.

OPTICAL, ELECTRICAL, AND MAGNETIC PROPERTIES OF MAGNESIUM OXIDE

ELECTRIC-FIELD-INDUCED CHANGES IN CONDUCTIVITY AND THERMAL BREAKDOWN IN MgO SINGLE CRYSTALS AT HIGH TEMPERATURES

R. A. Weeks K. F. Kelton[1]
E. Sonder J. C. Pigg

Prior measurements of the electrical conductivity of nominally pure MgO in the temperature range 1000 to 1700 K have shown that the conductivity is sample dependent, varying as much as an order of magnitude at 1300 K. Consequently, current flow has been attributed to a variety of carriers and mechanisms. Prominent among suggested conduction mechanisms is that of charge flow via positive-ion vacancies[2,3] which are assumed to be in excess because of trivalent cation impurities. It has recently been observed[4] that electric fields of moderate strength (about 1000 V cm^{-1}) applied at temperatures in the range 1273 to 1473 K reduce some trivalent impurities to their divalent state. We have now measured the effects of such electric fields applied at 1473 K on the conductivity and on the temperature dependence of conductivity. Results indicate that positive-ion vacancies are not the predominant charge carriers in the samples examined. Another surprising result of such treatments of MgO was that after treatments of several hours, during which conductivities of single crystal samples decreased, conductivities then began to increase to such an extent that catastrophic failure of the samples occurred.

The measurements were made in air with a three-probe (guarded) contact with a sample. Measuring voltages of 6, 12, and 22.5 V were used for σ determinations. The samples, 1-cm disks about 0.3 cm thick, were single crystals with platinum electrodes evaporated onto [100] crystal planes. Crystals were from two sources, the Norton Company and ORNL. The amount of impurities in the crystals, detected by emission spectroscopy, was about 500 ppm and about 200 ppm by weight in the Norton and in the ORNL crystals respectively.

The effects of electric-field treatment for times and temperatures corresponding to those found previously[4] to reduce the Fe^{3+} and other trivalent impurities are shown in Fig. 2.1 for one Norton and two ORNL samples. In this figure, the solid lines indicate the conductivity as a function of temperature

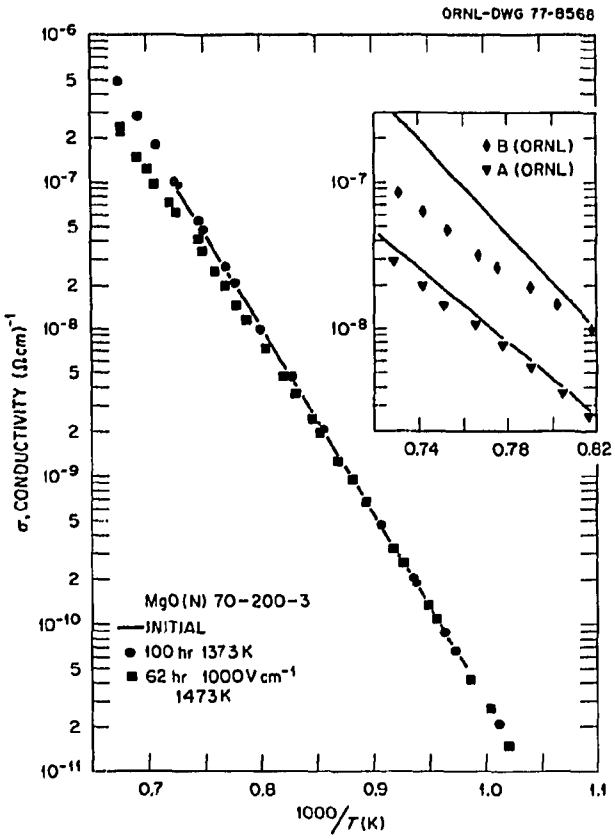

Fig. 2.1. Change of electrical conductivity of MgO due to electric-field treatment for times and temperatures necessary to reduce trivalent impurities. The curves indicate the behavior of the untreated samples. Circle points indicate annealing *in the absence of an electric field.* Squares, triangles, and diamonds are data obtained after treatment. Data for two ORNL samples are shown in an inset to prevent confusion.

for an untreated sample. The closed-circle symbols (for the Norton sample) show that for simple annealing, without the application of an electric field, neither the magnitude of the conductivity nor its temperature dependence is changed. However, after applying a field (*1000 V* cm^{-1}, *for about 20 hr at 1473* K), the conductivity at 1473 K decreased, as did the temperature dependence of the conductivity at lower temperatures. After this time, the conductivity changed relatively little for a period of about 100 hr. The temperature-dependent conductivity after 62 hr is shown in Fig. 2.1. It is clear that the conductivity at 1473 K is sample dependent, but in no case is it more than about a factor of 4. From previous work,[4] it is known that electric-field treatment of 20 to 50 hr decreases the amount of Fe^{3+} (Fe is the major impurity in these samples) by at least two orders of

magnitude. If this reduction had been accompanied by a corresponding decrease of positive-ion vacancies and if these were the predominant current carriers, then the conductivity should also decrease by more than two orders of magnitude. Thus it is unlikely that positive-ion vacancies are the predominant current carriers in MgO.

In the case of the Norton samples, electric-field treatment for times greater than about 100 hr produces an increase in conductivity at 1473 K. In the case of ORNL samples, an increase is also observed, but after different periods of time. For the Norton samples, the increase is approximately linear with time for many hours, after which the rate increases and thermal breakdown occurs. After breakdown, MgO samples exhibit dark-colored streaks extending from the cathode to the anode surface or from either surface towards the center of the sample. For one Norton sample, a hole connecting the cathode and anode surface could be seen after breakdown. This hole was embedded within a darkened region.

If the sample is cooled after the current has increased significantly, but before breakdown occurs, the formation of holes, but not of darkened areas, is prevented; the condition produced by approaching breakdown can be frozen in so that changes of conductivity due to that condition can be measured. The results of two such breakdown runs and the resulting conductivities are shown in Fig. 2.2. The heavy solid and dashed curves shown in Fig. 2.2 are a least squares fit of the data in Fig. 2.1 to the function $\ln \sigma = b - E/kT$. After the first and second breakdowns, the conductivity in the temperature range 900 to 1200 K increased approximately threefold and sixfold, respectively, while the slope E was, within error, unchanged. Upon heating above 1300 K, the enhanced conductivity began to disappear; and, after about 3 hr at 1470 K, the conductivity and its temperature dependence became similar to the dashed prebreakdown curve. After a 100-hr anneal at 1473 K, the conductivity and its temperature dependence, indicated by triangles, were in close agreement with the initial conductivity curve shown in Fig. 2.1. These results indicate that breakdown, as reported here, requires a lengthy incubation time. During this time, changes take place within the crystal that decrease its resistance to current flow, without significantly altering the activation energy. Moreover, microscopic investigations[5] of electric-field-treated samples show that ⟨100⟩ dislocation loops are produced in the vicinity of dislocations in the darkened regions. We suggest that the dislocation structure and the ⟨100⟩ loops in the samples are related to the breakdown phenomenon. We are thus led to the idea that current in MgO, particularly after electric-field treatment, flows along low-resistance filamentary paths (perhaps small-angle grain boundaries) and that, when these paths attain continuity between the cathode and anode to allow sufficiently large current flow, thermal breakdown takes place.

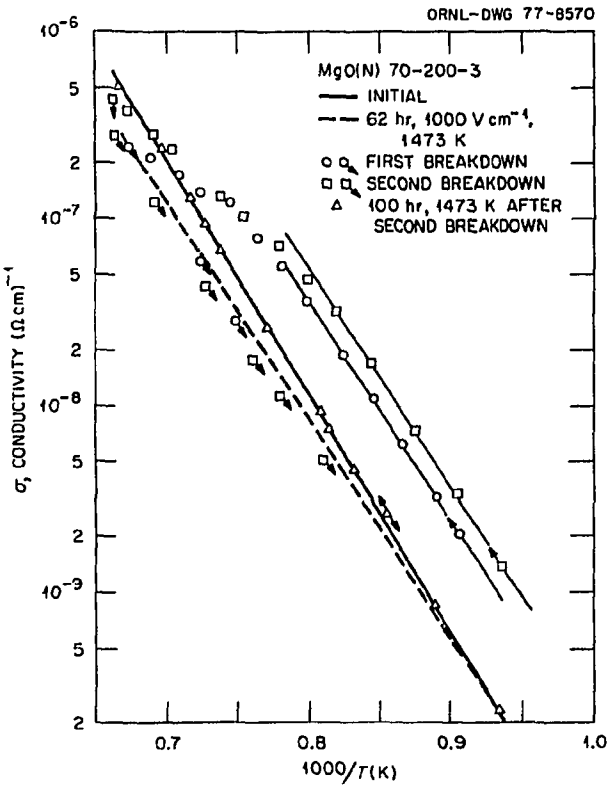

Fig. 2.2. Effect of extended electric field treatment of MgO. The heavy solid and dashed curves are fit to the data of Fig. 2.1. The circles and squares represent two consecutive treatments, each of which was interrupted before breakdown by cooling the sample and then taking data upon increasing and then decreasing the temperature as indicated by the arrows. The data represented by the triangles were obtained after a long anneal.

1. Summer research participant from the University of Tennessee, Knoxville.

2. C. B. Alcock and G. P. Stravropoulos, *J. Am. Ceram. Soc.* **54**, 436 (1971).

3. C. M. Osburn and R. W. Vest, *J. Am. Ceram. Soc.* **54**, 428 (1971).

4. R. A. Weeks et al., *J. Phys. (Paris), Suppl.* 37, 411 (1976).

5. J. Narayan, in *Proceedings of the Thirty-fifth Annual Meeting of Electron Microscopy Society of America*, ed. by G. W. Bailey, Claitor's Press, Baton Rouge, Louisiana (to be published).

$a\langle 100\rangle$ DISLOCATION LOOPS IN MgO

J. Narayan S. M. Ohr

Dislocation loops on {110} planes having $a/2\langle 110\rangle$ Burgers vectors introduced by plastic deformation and subsequent annealing of MgO have been studied extensively in the past using transmission electron microscopy.[1] Recently it was reported that high-temperature electrical conduction for a long period of time ($\geq$100 hr) induced a thermal breakdown[2] in MgO crystals. Transmission electron microscope investigation of these samples just before the thermal breakdown revealed the presence of a type of loop not previously observed in this material with $a\langle 100\rangle$ Burgers vectors lying in {100} planes.

Figure 2.3*a-d* shows electron micrographs of two of these $a\langle 100\rangle$ loops imaged with diffraction vectors (g) = [200], [020], [2$\bar{2}$0], and [$\bar{2}$20]. These micrographs were taken under kinematical diffraction conditions with the deviation parameter $w \sim 0.6$. From stereo microscopy it was determined that the loop labeled α lies in the (001) plane and hence is nearly parallel to the image plane and that the loop labeled β lies in the (100) plane and is viewed nearly edge-on. The image of loop α has two arcs, each consisting of a doublet and a line of no contrast. The doublet remains symmetrically displaced about the dislocation core for both plus and minus diffraction vector directions (Fig. 2.3*c* and *d*). This invariant behavior of the contrast with $\pm\mathbf{g}$ is characteristic of the $\mathbf{g}\cdot\mathbf{b} \times \mathbf{u}$ contrast with $\mathbf{g}\cdot\mathbf{b} = 0$ (where **b** and **u** are Burgers and tangent vectors of the loop respectively). The line of no contrast, which results from the portions of the loop where both $\mathbf{g}\cdot\mathbf{b}$ and $\mathbf{g}\cdot\mathbf{b}\times\mathbf{u}$ are zero, was found to be always perpendicular to the diffraction vector as shown in Fig. 2.3*a-d* for loop α. From this contrast behavior, the Burgers vector of loop labeled α is deduced to be a[001]. The small loop just to the left of loop α has $a/2$[011] Burgers vector and is of the type normally observed in this material. The loop β in Fig. 2.3*b* is out of contrast, except for the end-on images as dots which were shown to be invariant with $\pm\mathbf{g}$. As shown in Fig. 2.3*c* and *d*, the loop β

PHOTO 3503-77

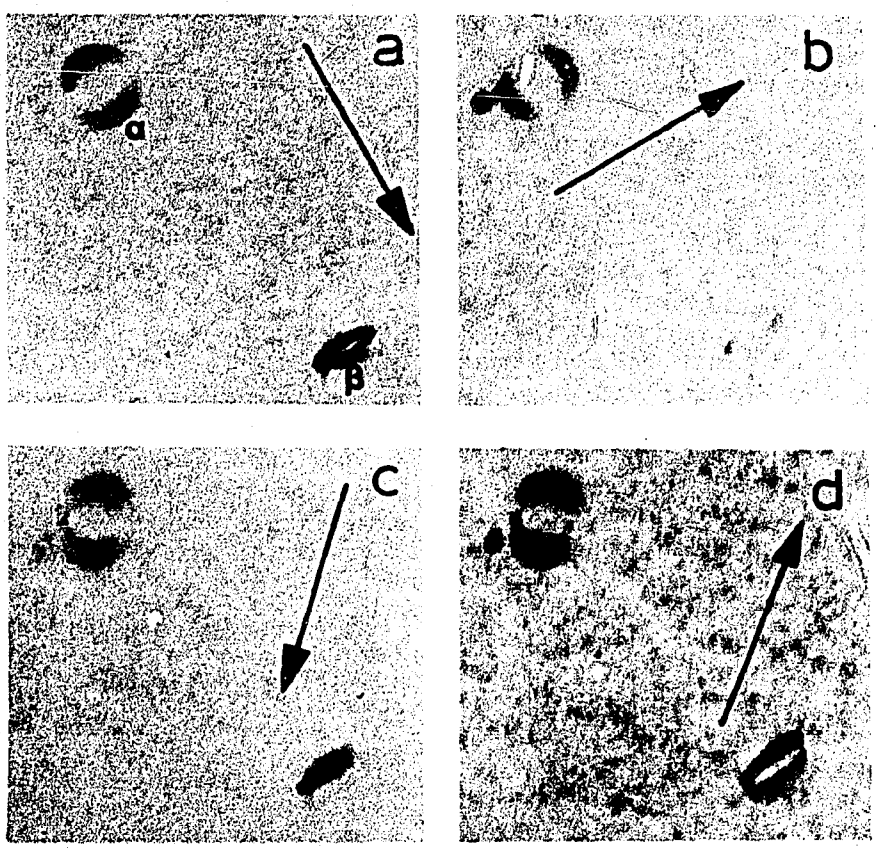

Fig. 2.3. Bright-field electron micrographs under kinematical diffraction conditions ($w \sim 0.6$). Arrows indicate the directions of diffraction vectors: (*a*) [200], (*b*) [020], (*c*) [2$\bar{2}$0], and (*d*) [$\bar{2}$20]; the length of the arrows is 0.3 μ.

PHOTO 3504-77

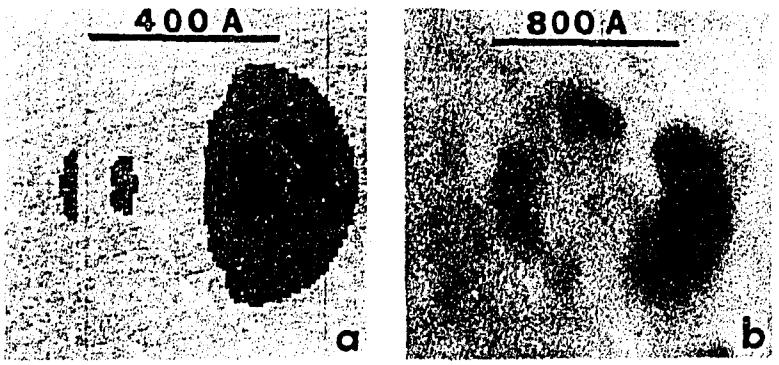

Fig. 2.4. Comparison of *(a)* computer simulated image of a 400 Å loop at a depth of 450 Å on (001) plane with *a*[001] Burgers vector under kinematical diffraction conditions ($w = 0.5$) and diffraction vector [200]; *(b)* electron microscope image of an 800 Å loop on (001) plane at a depth of 400 Å with $w \sim 0.6$ (black spot at the top of the figure is due to contrast from another small loop).

exhibits inside-outside contrast,[3] and the image is characteristic of $\mathbf{g}\cdot\mathbf{b} = 2$. This contrast behavior for loop β is expected if its Burgers vector is *a*[100]. Also, β-type loops were observed on (010) cube planes with *a*[010] Burgers vectors. The nature (vacancy or interstitial) of *a*[010] and *a*[100] dislocation loops was determined by the inside-outside contrast method. Ten each of *a*[010] and *a*[100] loops were analyzed, and all were found to be of a vacancy type.

A computer simulation of $\mathbf{g}\cdot\mathbf{b}\times\mathbf{u}$ image contrast of *a*⟨100⟩ loops has been performed. A typical example is shown in Fig. 2.4*a*. The simulated image shows the invariant contrast behavior of the two arcs with ±g; also shown is the line of no contrast, which is always perpendicular to g. An interesting new result which emerges from the simulation is that the contrast of the two arcs for a given loop is equal (i.e., the image is symmetrical, as in Fig. 2.3) only when the loop is situated more than two extinction distances ($>2\xi^g$, where ξ^g is the extinction distance corresponding to the diffraction vector used) from the foil surface or is near the transition boundaries ($0.5\xi^g$, $1.0\xi^g$, and $1.5\xi^g$). For those loops within two extinction distances of the surface, the contrast of one of the arcs is weaker (i.e., asymmetrical, as in Fig. 2.4*b*), and the vector from the stronger to the weaker arc (henceforth to be referred as m) is depth dependent. This depth dependence of the m vector is analogous to that of the *l* vector (black to white direction in the dynamical image contrast with $\mathbf{g}\cdot\mathbf{b}\neq 0$ of small loops) and can be used to identify the sense of Burgers vectors, that is, vacancy or interstitial nature of dislocation loops. The nature of *a*[001] loops was determined using the above rule and gave the same result as the inside-outside contrast method.

1. J. Narayan and J. Washburn, *Philos. Mag.* 26, 1179 (1972).
2. R. A. Weeks et al., *Proceedings of Conference on High-Temperature MHD Systems*, Argonne, Illinois, April 4-6, 1977 (in press).
3. D. M. Maher and B. L. Eyre, *Philos. Mag.* 23, 409 (1971).

REDUCTION OF IMPURITY IONS IN MgO BY CURRENT FLOW AT HIGH TEMPERATURE[1]

R. A. Weeks J. C. Pigg
E. Sonder K. F. Kelton[2]

It has been noted that the valence states of certain impurities in oxides can be changed by heating the samples in different gases or by passing currents through the base material at high temperatures.[3,4] With the hope of establishing the details of the mechanism by which electric currents cause valence changes, we have begun to study transition metal impurities in MgO, using a combination of electrical, optical, and electron paramagnetic resonance (EPR) measurements. The MgO crystals, results for which are described, contained approximately 200 ppm iron, 50 ppm manganese, 10 ppm each of vanadium and chromium, and larger amounts of aluminum and silicon. In a typical experiment a sample with a rather intense Fe^{3+} EPR spectrum was annealed at about 1000°C for about 100 hr with or without an applied electric field. Without a field there was little change in

the Fe^{3+} EPR line intensities. With an electric field of about 1000 V/cm, more than an order of magnitude *decrease* in the Fe^{3+} spectra occurred. In addition to the changes in the Fe^{3+} spectra, the spectra of Cr^{3+} decreased while those of V^{2+} increased. There was no evidence of any effect on Mn^{2+}.

Other experiments show that the reduction process is accompanied by the creation of defects that act as shallow electron traps and that the reduction is not uniform throughout the MgO samples, proceeding from the negative towards the positive electrode.

1. Summary of paper: *J. Phys. (Paris), Suppl.* 37, 411 (1976).
2. Summer research participant from the University of Tennessee, Knoxville.
3. R. L. Hansler and W. G. Segelken, *J. Phys. Chem. Solids* 13, 124 (1960).
4. M. G. Harwood, p. 221 in *Electrical Conductivity of Rutile III and IV, Special Ceramics 1964*, ed. by P. Popper, Academic Press, London, 1965.

DETERMINATION OF THE Fe^{2+} AND Fe^{3+} CONCENTRATION IN MgO[1]

F. A. Modine E. Sonder R. A. Weeks

Crystals of MgO containing 140 ppm iron were reduced in CO or oxidized in air at 1150°C, and the iron concentration in different valences was determined by optical and magnetic techniques. Optical density, electron spin resonance, and magnetic circular dichroism measurements gave self-consistent results that yielded calibration constants for determining the Fe^{2+} and Fe^{3+} concentrations by optical means. These constants given in Table 2.1 may be used generally to extract Fe^{2+} and Fe^{3+} concentrations from measured values of optical density or magnetic circular dichroism. Oscillator strengths of the 1000- and 285-nm absorption bands were calculated from the iron concentrations in the 2+ and 3+ valence states. They are compared with previously determined values in Table 2.2. At the relatively low concentrations studied (~140 ppm), more than 90% of the iron is unassociated Fe^{2+} or Fe^{3+}. Alternate oxidation with air and reduction with CO converted 80% of the unassociated iron between 2+ and 3+ valence states, while the other 20% always remained as Fe^{2+}.

1. Summary of paper to be published.

Table 2.2. Oscillator strengths of MgO iron bands

Optical band	Oscillator strength	Source
Fe^{2+}: 1000 nm	7.3×10^{-6}	This work
	$(3\text{-}5) \times 10^{-5}$	Manson et al.
	5×10^{-6}	Hjortsberg
Fe^{3+}: 285 nm	3.8×10^{-2}	This work
	4.1×10^{-2}	Davidge
	1.4×10^{-2}	Sibley et al.

Sources:
N. B. Manson et al., *J. Phys. Chem. Solids* 37, 1145 (1976).
A. Hjortsberg, Thesis, Chalmers University of Technology, Goteborg (1975); *Bull. Am. Phys. Soc.* 21, 421 (1976).
R. W. Davidge, *J. Mater. Sci.* 2, 339 (1967).
W. A. Sibley, J. L. Kolopus, and W. C. Mallard, *Phys. Status Solidi* 31, 223 (1969); Y. Chen and W. A. Sibley, *Phys. Rev.* 154, 842 (1967).

Table 2.1. Proportionality constants for calculating Fe^{2+} and Fe^{3+} concentrations in MgO from optical measurements[a]

Valence	Measurement wavelength (nm)	Dichroism (weight, ppm/cm^{-1})	Absorption (weight, ppm/cm^{-1})
Fe^{2+}	1000	$(9.1 \pm 1.5) \times 10^{1}$	$(4.8 \pm 0.6) \times 10^{1}$
Fe^{3+}	285	15 ± 2	2.0 ± 0.3

[a]The constants are appropriate for low temperature. Dichroism constants are scaled to saturation, but may be scaled to any temperature with the appropriate Brillouin function.

AN INVESTIGATION OF THE REOXIDATION PROCESS OF AN ELECTROLYTICALLY REDUCED MgO CRYSTAL

Christopher Levey[1] E. Sonder
R. A. Weeks

Single crystals of MgO, in which the trivalent impurities have been reduced through the application of an electric field of about 1000 V/cm at temperatures up to 1275°C, are used to study the Fe^{2+} oxidation process. By annealing the crystals in air at 1150°C for 164 hr and monitoring the 2830 Å Fe^{3+} absorption band as a function of position within the crystal, the concentration of Fe^{3+} is found to decrease from the surface to the center of a crystal cube. A diffusion coefficient on the order of 10^{-6} cm^2/sec is found for the reoxidation process. An activation energy determination for the process appears to be feasible.

1. ORAU undergraduate research trainee from Carlton College, Northfield, Minn.

RADIATION-INDUCED DIFFUSION OF HYDROGEN AND DEUTERIUM IN MgO[1]

Y. Chen M. M. Abraham H. T. Tohver[2]

Mass transport of ions in insulating compounds during irradiation has been a much neglected field of study. Little, if any, work has been done in the high-temperature oxides. We report a new phenomenon of high diffusivity for substitutional hydrogen and deuterium in MgO under electron irradiation. It establishes that the usual diffusion constants for hydrogen, deuterium, and (by implication) tritium cannot be used to predict the behavior of these isotopes in insulators under irradiation, as can be done, for example, in controlled thermonuclear applications.

The O-H and O-D stretching frequencies corresponding to several configurations in MgO have been identified in the past.[3] In particular, the absorption bands at 3296 and 2445 cm^{-1} have been convincingly attributed to H^+ or D^+, respectively, substituting for Mg^{2+} ions. The H^+ or D^+ in this site is affected by covalent bonding to one of the six neighboring oxygen ions, and the resultant lattice distortion yields the following configuration:

$$Mg^{2+} - OH^- - [\text{Mg vacancy}] - O^{2-} - Mg^{2+}.$$

Rapid quenching from high temperature (>1300 K) maximizes the substitutional hydrogen and minimizes the formation of $Mg(OH)_2$ precipitates, which absorb at 3700 cm^{-1}. Slow cooling from elevated temperatures has the reverse effect.

An MgO crystal containing only hydrogen was first quenched from 1450 K into a liquid-nitrogen bath. Subsequent isochronal annealing measurements indicated that the absorption coefficient, α, of the 3296-cm^{-1} band remained constant until the annealing temperature (T_A) reached about 800 K. With further increase in temperature, α decreased until $T_A \cong 850$ K, beyond which it increased. The pertinent result is that the hydrogen ions are thermally stable and are incapable of escaping from substitutional sites at temperatures under 800 K.

Following electron irradiations, the situation is different: The photon absorption decreased with irradiation dose. The effect on the 3296-cm^{-1} band amplitude due to electron irradiations at $T \cong 85$ and 290 K is illustrated in Fig. 2.5. The decrease in absorption at the higher temperature was much more rapid. For both irradiations, the decrease in the band intensity was attended by the enhancement of a broad optical absorption band at 2.3 eV (540 nm) and the appearance of an infrared band at about 3700 cm^{-1}.

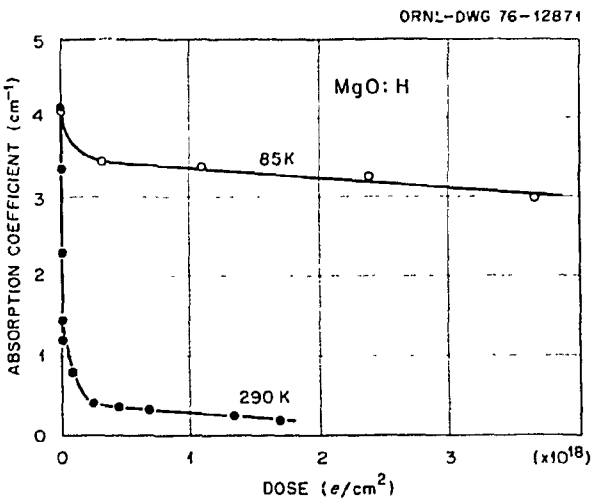

Fig. 2.5. Decay of the 3296-cm^{-1} absorption band in MgO:H as a function of electron dose for two irradiation temperatures.

The 2.3-eV band is due to the V_3 center, which is a magnesium vacancy with a trapped hole on a neighboring oxygen. Therefore, electron irradiation has the effect of displacing the substitutional hydrogen, which subsequently migrates to aggregate at precipitates, leaving a magnesium vacancy behind. From the slope of the curve for the 290 K irradiation in Fig. 2.5, a cross section of about 3×10^8 b was obtained. For the 85 K irradiation, a value of about 10^6 b was determined.

A crystal containing both hydrogen and deuterium was used for a comparison of their displacement probabilities. The advantage of using one crystal is that the experimental conditions for displacement, temperature, beam intensity, and dose are identical for both hydrogen and deuterium. The ratio of the absorption coefficient after each irradiation to that prior to irradiation, α/α_0, is plotted for both the 3296- and 2445-cm^{-1} bands in Fig. 2.6. The decay of the former is more rapid than the latter. Hence we conclude that hydrogen is displaced more readily than deuterium.

The enormous cross section for the radiation-induced displacement, or diffusion (RID), of hydrogen (and/or deuterium) from the substitutional site appears to have no precedent. An analog of this phenomenon is radiation-enhanced diffusion (RED) in metals, which is caused by the increased atomic interchange resulting from radiation-produced defects, such as interstitials and vacancies. Whereas RED in metals is a manifestation of defects created as a result of knock-on damage, RID of hydrogen in MgO is a result of the ionizing property of the incident electrons, *independent* of whether defects are created in the crystal or not. Furthermore, the RID of hydrogen proceeds with a rapidity incompatible with possible RED in MgO, since the latter process requires knock-on damage for initiation.

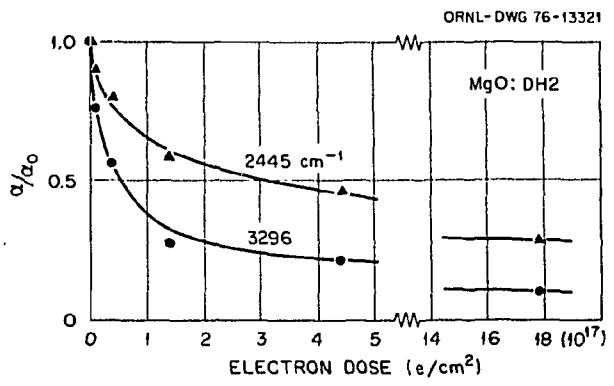

Fig. 2.6. Normalized decay of 3296-and 2445-cm^{-1} bands under electron irradiation for sample MgO:DH2.

1. Summary of paper: *Phys. Rev. Lett.* 37, 1757 (1976).
2. On leave from the University of Alabama, Birmingham.
3. See a recent review, Y. Chen and M. M. Abraham, *New Phys.* 15, 47 (1975).

STABLE [Li]^0 DEFECTS IN MgO SINGLE CRYSTALS[1]

M. M. Abraham L. A. Boatner[2]
Y. Chen R. W. Reynolds[3]

The addition of lithium to MgO results in a significant suppression of radiation damage in this material, and in view of the interest in using MgO as an electrical insulator in high-radiation environments, the problem of understanding the solid state processes in the lithium magnesium oxide system assumes new importance.

The [Li]^0 defect, which is a substitutional Li^+ ion with a hole trapped at a neighboring oxygen site, has a low-temperature EPR spectrum, which is due to three inequivalent sites possessing tetragonal symmetry with the principal axes lying along ⟨100⟩ crystallographic directions. Formed by low-temperature irradiations, the centers have been observed to annihilate upon warming to room temperature via hole release.

The present work demonstrates that it is possible to form a stable [Li]^0 center in MgO:Li by means of a rapid quench from 1500 K or by high-dose electron irradiations at room temperature. An electron nuclear double resonance (ENDOR) investigation of the stable [Li]^0 center formed by rapid quenching of the sample was performed at a temperature of 4.2 K. The ENDOR spectra appeared to be exactly the same as those obtained for the radiation-induced defect. The stable [Li]^0 center may be either destroyed by slowly cooling the MgO crystal from 1500 K or regenerated by reheating the sample and repeating the quenching process. The optical absorption spectra corresponding to the three ways of generating [Li]^0 centers are illustrated in Fig. 2.7. Optical bands, the most pronounced of which occurs at 1.83 eV, were created as a result of a short ionizing electron irradiation at about 80 K, shown in spectrum *a*. These bands were unstable at room temperature. The same crystal, quenched from 1500 K, resulted in a more intense 1.83-eV band, spectrum *c*, which is stable even at $T \gg 295$ K. Another MgO:Li crystal,

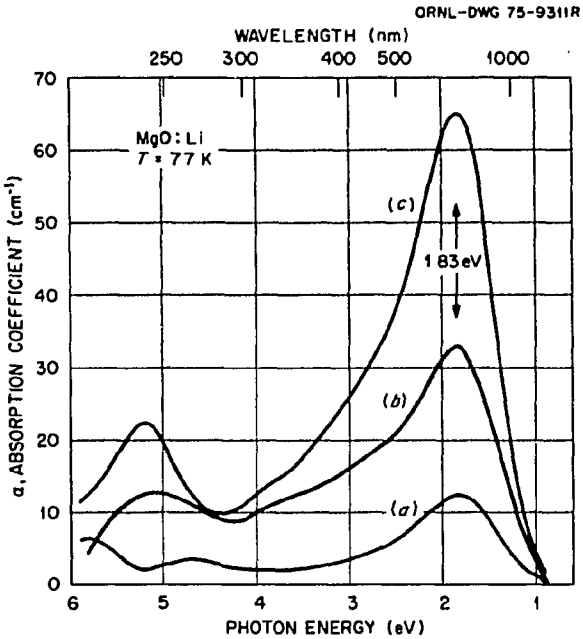

Fig. 2.7 Optical spectra of Li-doped MgO crystals: curve *a*, irradiated with a short ionizing dose of electrons at 80 K; curve *b*, irradiated to 5×10^{18} electrons/cm^2 at 295 K; and curve *c*, quenched from 1500 K.

irradiated to a dose of 5×10^{18} electrons/cm^2 at room temperature, yielded spectrum *b*. Again a stable band is observed at 1.83 eV. The effects of quenching from high temperature or irradiation to large electron doses are reproducible in other MgO:Li crystals. It is believed that the 1.83-eV band is due to the optical transition of the $[Li]^0$ center by virtue of the observed large absorption half-width and peak wavelength which is expected of monovalent alkali metal trapped-hole centers.[4] This is confirmed by the parallel behavior of the band and the EPR $[Li]^0$ signal in the three situations indicated in this figure. Additionally, Modine has unequivocally established this correlation using a magnetic-circular-dichroism EPR double resonance technique.[5]

Before a definitive model for the different processes involved in the formation of the stable and unstable $[Li]^0$ centers can be formulated, additional investigations are necessary.

1. Summary of paper: *Phys. Rev. Lett.* 37, 849 (1976).
2. Ecole Polytechnique Federale de Lausanne, Lausanne, Switzerland.
3. Advanced Technology Center, Dallas, Tex. Present address: General Research Corporation, Huntsville, Ala.
4. For a recent review of the properties of trapped-hole defects in MgO, see Y. Chen and M. M. Abraham, *New Phys.* 15, 47 (1975).
5. F. A. Modine, "Magneto-Optical Properties of $[Li]^0$ Defects in MgO," this report.

MAGNETO-OPTICAL PROPERTIES OF $[Li]^0$ DEFECTS IN MgO[1]

F. A. Modine

A study was made of the magnetic circular dichroism (MCD) and optically detected EPR spectra of $[Li]^0$ centers produced by the thermal quenching of MgO:Li from approximately 1200°C ($[Li]^0$ centers are electron holes trapped at substitutional Li^+ ions). The spectra affirm that $[Li]^0$ centers produce the optical absorption that is observed in quenched MgO:Li. A theoretical analysis of the MCD spectrum has important implications regarding the various models that have been proposed to explain the electronic structure of trapped holes in alkaline-earth-oxide crystals.

Figure 2.8 shows MCD and optical density (OD) spectra of MgO containing $[Li]^0$ centers. The

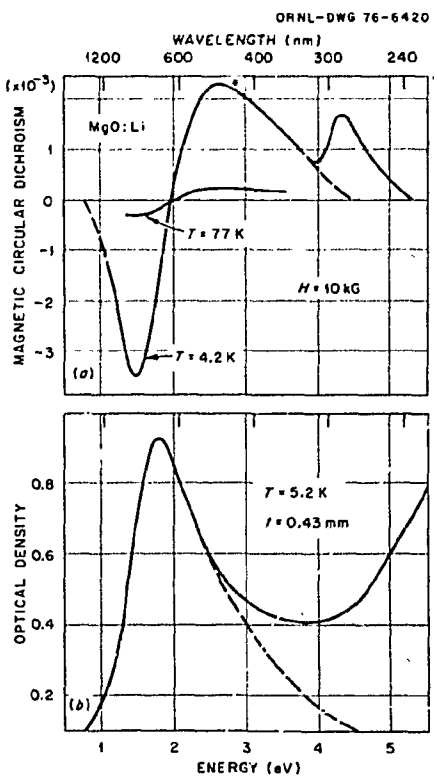

Fig. 2.8. Optical spectra of a thermally quenched crystal of MgO:Li. The magnetic circular dichroism is the difference between the absorption of left and right circularly polarized light. Dashed curves represent decompositions or extrapolations. The MCD at 4.3 eV is attributed to Fe^{3+}. Units are base 10 absorbance.

resolution of the absorption band from the background is suggested by the MCD spectrum and also by the difference between absorption spectra that were measured as a function of defect concentration. The MCD has a strongly temperature-dependent intensity and an approximately absorption-derivative-like shape which reveal that the spectrum derives from the combined effect of ground-state spin polarization and excited-state spin-orbit coupling. An Fe^{3+} charge-transfer band at 4.3 eV has little OD, but it does contribute significant MCD. The resolution of the $[Li]^0$ and Fe^{3+} MCD is based upon a spectrum measured[2] for MgO:Fe. Figure 2.9 shows optically detected EPR spectra which verify that the MCD is primarily due to $[Li]^0$ centers. The $[Li]^0$ EPR is seen as a decrease in the MCD intensity. The reduction is nearly uniform (40 ± 3% for the spectrum of Fig. 2.9) except at shorter wavelengths where Fe^{3+} contributes. No MCD from other defects or impurities was detected.

A comprehensive analysis of the optical spectra was based upon the theory of moments, and the results of the analysis were compared with the predictions of models that have been proposed to explain the electronic structure of the alkaline-earth-oxide trapped-hole centers. These models are (*a*) the ion model of Bartram et al.,[3] in which optical transitions are between the Stark-split $2p$ levels of a single O^- ion; (*b*) the delocalized-hole model of Izen et al.,[4] in which transitions are between molecular orbitals constructed as LCAO's from O^{2-} $2p$ orbitals; (*c*) the polaron model of Schirmer et al.,[5] in which the transitions occur between the vibronic potential wells that correspond to hole localization in the σ orbitals of different O^{2-} ions; and (*d*) the mixed ion and polaron model of Norgett et al.,[6] in which both the ion- and polaron-model transitions contribute significantly to the optical band. The significant conclusions are as follows. Contrary to conclusions of Izen et al.,[4] the ion model gives a qualitative explanation of the trapped-hole MCD spectra. Although the ion-model explanation has been refuted by different studies,[7] this result is significant because it advances the mixed ion- and polaron-model explanation. A polaron-model explanation of the MCD was found completely unfeasible unless the model was modified by assuming a significant π-orbital contribution to the excited-state wave functions. A qualitative, but not a quantitative, interpretation of the MCD spectrum was obtained

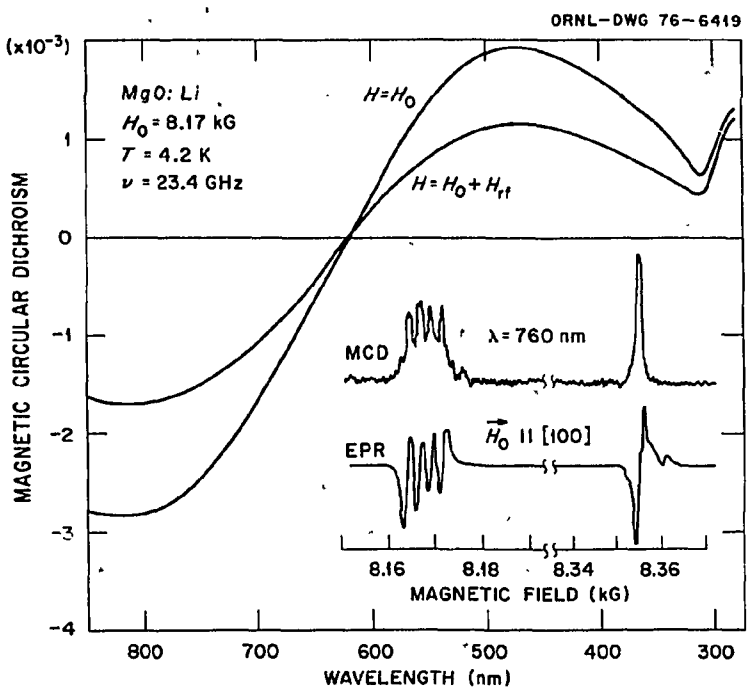

Fig. 2.9. The MCD spectrum measured with and without microwave power and using a magnetic field that enabled the $[Li]^0$ perpendicular EPR lines to be observed on an oscilloscope when power was applied. The insets show the EPR measured as the derivative of microwave power absorption and as the concomitant change in the MCD.

for the polaron model when a configurational and magnetic-field-induced admixture of π orbitals was assumed. A quantitative explanation of the MCD based upon any of the existing models appears to require stronger magnetic interactions than are expected for the orbitals on O^- ions.

1. Summary of paper: *Solid State Commun.* 20, 1097 (1976).
2. F. A. Modine, E. Sonder, and R. A. Weeks, "Determination of the Fe^{2+} and Fe^{3+} Concentration in MgO," this report.
3. R. H. Bartram, C. E. Swenberg, and J. T. Fourier, *Phys. Rev.* A 139, 941 (1965).
4. E. H. Izen, R. M. Mato, and J. C. Kemp, *J. Phys. Chem. Solids* 34, 1431 (1973).
5. O. F. Schirmer, P. Koidl, and H. G. Reik, *Phys. Status Solidi B* 62, 385 (1974).
6. M. J. Norgett, A. M. Stoneham, and A. P. Pathak, *J. Phys. C* 10, 555 (1977).
7. F. A. Modine, "Stress-Induced Optical Dichroism of $[Li]^0$ Defects in MgO," this report.

STRESS-INDUCED OPTICAL DICHROISM OF $[Li]^0$ DEFECTS IN MgO[1]

F. A. Modine

A study was made of the stress-induced optical dichroism of $[Li]^0$ centers that are produced by quenching MgO:Li from high temperature. A theoretical treatment of the dichroism by the method of moments was developed, and an analysis of the data gave information regarding both the electronic structure and the local crystal environment of this center.

The $[Li]^0$-center optical spectra are shown in Fig. 2.10. Because the OD spectrum is not well resolved from the background, the true shape of the band was estimated from a comparison of the MCD of the band with the MCD of a better resolved band in another sample[2] and also from the OD spectra reported by Abraham et al.[3] The dichroism spectrum has a mixed absorption-like and absorption-derivative-like shape which reveals that the excited state contains levels having different symmetry. From EPR studies,[4] the $[Li]^0$ ground-state symmetry is known to be A_1 of the C_{4v} point group, and the dichroism reveals that the higher and lower energy portions of the absorption spectrum are predominantly of A_1 and E symmetry respectively.

The strong temperature dependence of the dichroism reveals that it originates predominantly in

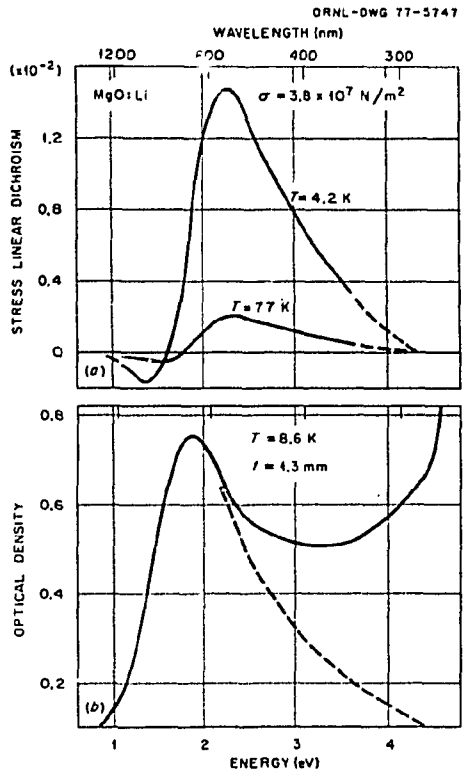

Fig. 2.10. Optical spectra of a thermally quenched crystal of MgO:Li. Dashed curves represent decompositions or extrapolations. The dichroism is the difference between the absorption of light polarized perpendicular and parallel to the stress axis. Units are base 10 absorbance.

the stress-induced alignment of an inherently dichroic defect. The dichroic anisotropy of the defect can be described by a ratio of transition-dipole strengths, $D_\parallel / D_\perp \cong 2.2$, and an energy splitting, $E_\parallel - E_\perp \approx 0.37$ eV, for light polarized parallel ($\parallel$) and perpendicular ($\perp$) to the defect symmetry axis. These results correspond well to predictions of the polaron model of the defect,[3] and no evidence for an ion-model contribution[2] to the optical band was found.

Figure 2.11 shows the stress and temperature dependence of the 500-nm peak dichroic intensity. Because the dichroism is not a function of σ/T, it does not derive from Boltzmann factors that are functions only of stress (σ) and temperature (T). Apparently there are internally generated stress or electric fields in the crystal that tend to pin the defects into random orientations at low temperature. A statistical analysis reveals that the low-temperature

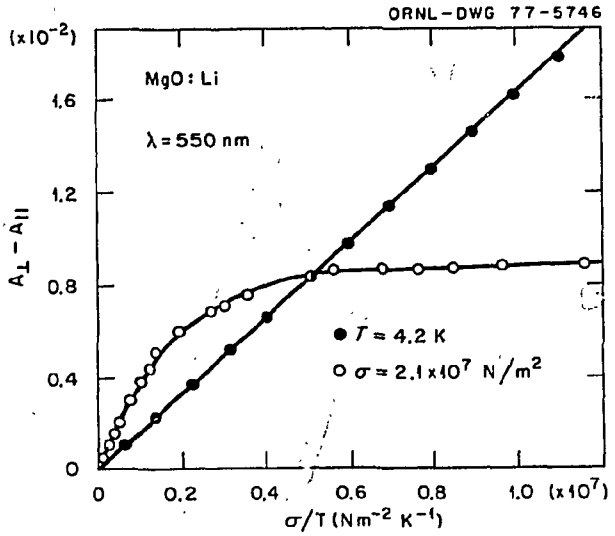

Fig. 2.11. The stress (σ) and temperature (T) dependence of the peak dichroism. The solid curves are from theory which assumes a randomly distributed electric field described by the effective temperature $T_e \approx 13.5$ K.

behavior of the dichroism can be satisfactorily attributed to random electric fields, which are caused by randomly distributed charged point defects.

1. Summary of paper to be published.
2. F. A. Modine, "Magneto-Optical Properties of $[Li]^0$ Defects in MgO," this report.
3. M. M. Abraham et al., "Stable $[Li]^0$ Defects in MgO Single Crystals," this report.

EVIDENCE FOR SUPPRESSION OF RADIATION DAMAGE IN Li-DOPED MgO[1]

Y. Chen M. M. Abraham

The availability of materials which are relatively resistant to radiation damage is essential for modern energy conversion devices. Most impurities in crystalline solids have been shown to enhance radiation-induced defect production, presumably by the trapping of displaced interstitials. The present work reports the first experimental evidence that an impurity in an oxide (in this case, lithium in MgO) suppresses the production of anion vacancies and divacancies.

Elastic collisions of energetic particles with lattice ions produce vacancies in the crystal. The maximum recoil energy of an indigenous oxygen ion from a collision with a 1-MeV neutron is 4.4×10^5 eV, compared to 6.8×10^2 eV from collision with a 1.8-MeV electron. Consequently, whereas electron irradiations produce primarily anion vacancies, neutron irradiations produce a variety of defects, such as divacancies and cluster defects, in addition to anion vacancies. In this investigation, the principal method of identifying defects and measuring their concentration was optical absorption spectroscopy. To supplement the optical data, EPR and ENDOR measurements were also used.

For electron irradiations, a dose of 3×10^{18} electrons/cm^2 produced an anion-vacancy concentration of 1×10^{17} cm^{-3} in the undoped MgO crystals and an undetectable concentration in the MgO:Li crystals. In the latter, however, an optical band at 1.83 eV was produced. This band was due to the $[Li]^0$ center, a substitutional lithium ion with a hole trapped at a neighboring oxygen site.

Figure 2.12*a* shows spectra from a variety of defects produced in undoped, neutron-irradiated MgO. The most pronounced peak, observed at 4.95 eV, indicated copious anion vacancies. Three other peaks were observed at approximately 3.5, 2.2, and 1.3 eV. At low temperatures, the broad bands at 3.5

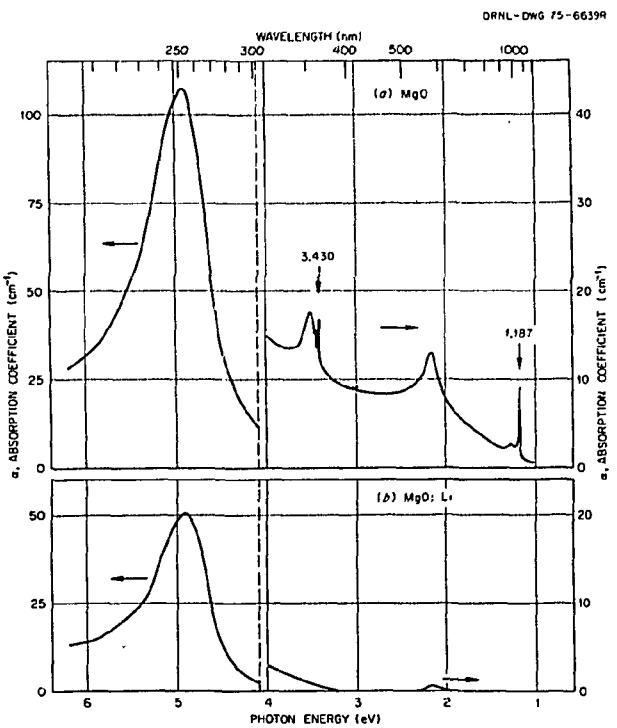

Fig. 2.12. Optical absorption spectra at 77 K of (*a*) nominally pure and (*b*) Li-doped MgO crystals, both irradiated to a dose of 6.4×10^{16} neutrons/cm^2. Atomic absorption measurement of doped crystal indicated the presence of 0.056 at. % lithium.

and 1.3 eV were attended by zero-phonon lines at 3.430 and 1.187 eV respectively. Previous studies have attributed these bands and zero-phonon lines to optical transitions within the anion divacancy.[2-4] Figure 2.12*b* illustrates the absorption spectrum of a Li-doped MgO crystal, neutron-irradiated simultaneously to the same total dose as the pure crystal whose spectrum is shown in Fig. 2.12*a*. The anion-vacancy band at 4.95 eV was reduced by a factor of 2 and the band at 2.2 eV by a factor of 6 in MgO:Li. The anion divacancies appeared to be completely suppressed in the Li-doped crystals.

The results of this investigation indicate that, for both electron and neutron irradiation, at ambient temperature the net production of intrinsic point defects is inhibited by the lithium doping of MgO.

1. Summary of paper: *J. Am. Ceram. Soc.* **59**, 101 (1976).
2. I. K. Ludlow, "Symmetry of a Color Center in Magnesium Oxide," *Proc. Phys. Soc., London*, 88(3), 763 (1966).
3. Y. Chen and W. A. Sibley, "Study of Zero-Phonon Lines in Electron-Irradiated, Neutron-Irradiated, and Additively Colored MgO," *Philos. Mag.* 20(164), 217 (1969).
4. Y. Chen, "Evidence of Anion Divacancies in MgO," Abstract C44 in *Proceedings of the International Conference on Colour Centers in Ionic Crystals*, Reading, United Kingdom, 1971.

IONIC CONDUCTIVITY AND SUPERCONDUCTIVITY

VIBRATIONAL SPECTROSCOPY OF SODIUM BETA-ALUMINA[1]

R. Frech[2] J. B. Bates

Raman, infrared reflectivity and emissivity spectra of single crystal sodium beta-alumina (Naβ-Al_2O_3) have been measured in the region of the internal and external optic phonons at temperatures from 12 to 1000 K to provide a basis for understanding the lattice dynamics of this material. A survey of the polarized Raman spectra of Naβ-Al_2O_3 is shown in Fig. 2.13. The $a(cc)a'$ spectrum arises from A_{1g} modes (D_{6h} group) in which the induced dipole moments are perpendicular to the conduction plane, while the $a(a'a')c$ spectrum is due to A_{1g} modes in which the moments are parallel to this plane. The E_{1g} modes are active in the $a(ca)c$ spectrum, and the E_{2g} modes are active in the $a(a'a)c$ spectrum.

A refinement[3] of the crystal structure of Naβ-Al_2O_3 showed that the space group is D_{6h}^4. The irreducible representations for the $k = 0$ optic

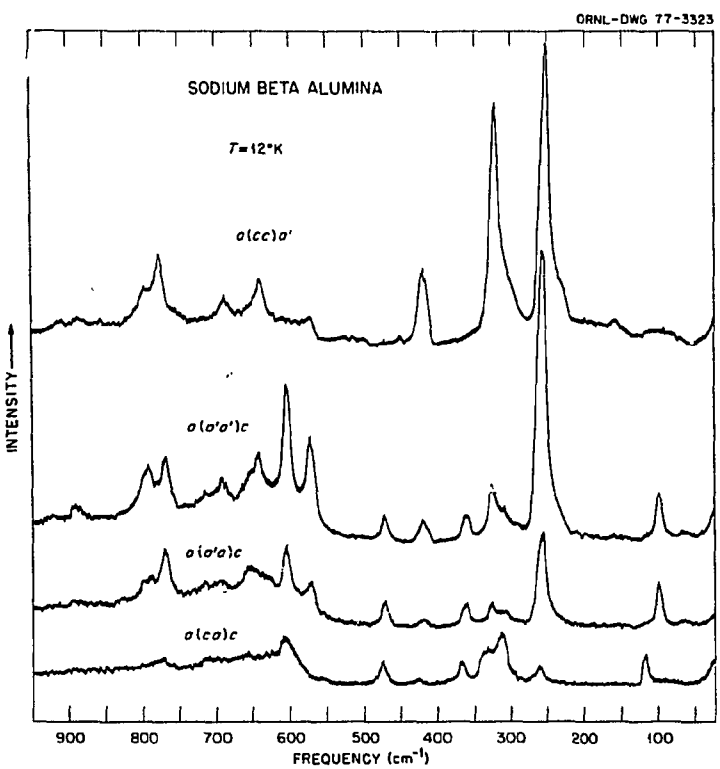

Fig. 2.13. Polarized Raman spectra of sodium beta-alumina measured at 12 K.

modes predict 42 Raman active modes ($11A_{1g} + 14E_{1g} + 17E_{2g}$) and 30 infrared active modes ($13A_{2u} + 17E_{1u}$). If only the atoms in the spinel blocks are considered, these are reduced to 37 Raman modes ($10A_{1g} + 13E_{1g} + 14E_{2g}$) and 25 infrared modes ($11A_{2u} + 14E_{1u}$). The observed Raman spectrum, however, contained only 23 Raman lines which could be attributed to vibrations of the spinel block. A schematic representation of the Naβ-Al_2O_3 lattice, viewed perpendicular to the c axis, is shown in Fig. 2.14*a*. The layers of the spinel blocks are joined through an oxygen atom in the conducting plane. Because the coupling between adjacent layers must be weak, it is reasonable to assume that the vibrations within a layer are localized. As shown in Fig. 2.14, if the conducting planes are ignored, the structure of Naβ-Al_2O_3 may be represented by interpenetrating layers of spinel blocks. On removing alternate layers, the lattice collapses to a structure in which a single block outlined in Fig. 2.14*b* becomes the primitive unit cell. It can be shown that this "reduced" structure belongs to the space group D_{3d}^3. Based on this new space group, the irreducible representations predict 23 Raman active modes ($10A_{1g} + 13E_g$) and 23 infrared active modes ($10A_{2u} + 13E_u$). The selection rules for the reduced structure are in excellent agreement with the observed spectra. Therefore, neglecting interactions between spinel blocks is a good approximation in developing a model to describe the internal modes of Naβ-Al_2O_3.

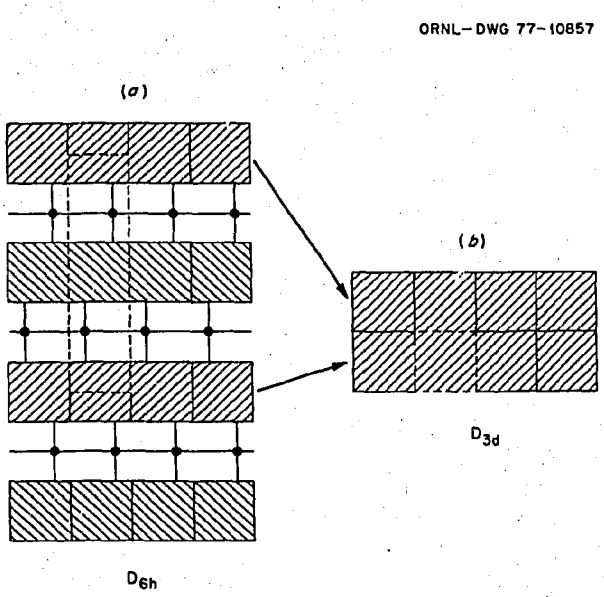

Fig. 2.14. Schematic diagrams of the full and the reduced lattice structures of sodium beta-alumina. The shaded and cross-hatched areas represent alternate layers of spinel blocks. Columnar oxygens in the conducting plane are represented by the solid circles. The dashed outlines give the boundaries of (*a*) the D_{6h} unit cell, and (*b*) the D_{3d} unit cell.

1. Summary of paper to be published.
2. ORAU summer faculty participant from the University of Oklahoma, Norman.
3. C. R. Peters et al., *Acta Crystallogr., Sect. B* 27, 1826 (1971).

ELECTRON PARAMAGNETIC RESONANCE OF IRRADIATED SODIUM BETA-ALUMINA

H. J. Stapleton[1] Y. Chen
H. T. Tohver[2] M. M. Abraham

When subjected to ionizing radiation at low temperature, the solid electrolyte sodium beta-alumina exhibits a paramagnetic center with axial symmetry about the crystallographic c axis. After the sample was γ-irradiated at 77 K, its EPR spectrum was measured at 177 K with a microwave frequency at 9.1 GHz. With the external magnetic field parallel to the c axis, the EPR absorption line was a broad (43 G peak-to-peak derivative linewidth), symmetric, and structureless signal centered at $g_{\parallel} = 2.048(5)$. When the magnetic field was perpendicular to the c axis, that is, in the plane of ionic conduction, the signal was resolved into 10 to 12 sharp, equally spaced hyperfine lines of unequal intensities. These were centered at a $g_{\perp} = 2.002(9)$ and separated by approximately 7.5 G. Total linewidth in this orientation was slightly greater (50 G peak-to-peak derivative) than the parallel orientation, and a weaker resonance line overlapped the low-field side of the spectrum.

These g values indicate that the paramagnetic center probably involves a hole. The complex hyperfine structure, observed in the perpendicular orientation, suggests that the interaction involves either three equivalent sodium ($I = {}^3/_2$) nuclei or two equivalent aluminum ($I = {}^5/_2$) nuclei. Several attempts to identify the nuclei involved were made using the technique of ENDOR at liquid helium temperatures, but no ENDOR signals could be observed.

Isochronal annealing measurements between 117 K and room temperature, using 6-min heating

periods, indicate that the paramagnetic center is stable to about 225 K, and then near 250 K the concentration drops to one-half the original value.

1. On leave from the University of Illinois, Urbana.
2. On leave from the University of Alabama, Birmingham.

OPTICAL ABSORPTION AND THERMOLUMINESCENCE OF IRRADIATED SODIUM BETA-ALUMINA

H. T. Tohver[1] M. M. Abraham
H. J. Stapleton[2] Y. Chen

Optical absorption bands were created when a sodium beta-alumina crystal was given a short ionizing irradiation at 80 K. Isochronal annealing of the crystal resulted in a decrease in the band intensities and emergence of other absorption bands, indicating that an electronic transfer process was involved. For this reason, spectral thermoluminescence measurements were studied in conjunction with isochronal annealing of optical absorption. The same crystal on which the electron paramagnetic resonance work was performed was also used for these optical studies.

After the crystal was electron-irradiated to a dose of 5×10^{16} electrons/cm^2 at 80 K, two optical absorption bands were observed at 2.44 and 4.86 eV. With the sample maintained at 80 K, both bands decayed slowly with time. Concomitant with this decay at 80 K, two thermoluminscence peaks were observed at 3.45 and 1.75 eV. The latter was a sharp line attended by fine structure, suggesting an electronic transition at an impurity. With isochronal annealing between 160 and 200 K, the 2.44-eV absorption band decreased in intensity and shifted toward 2.53 eV. Upon annealing at 230 K, a new absorption band at 3.28 eV emerged. Near room temperature, all these radiation-induced bands rapidly diminished in intensity. The thermoluminescence peak at 1.75 eV persisted to room temperature, reaching a peak emission intensity at 230 K.

1. On leave from the University of Alabama, Birmingham.
2. On leave from the University of Illinois, Urbana.
3. H. J. Stapleton et al., "Electron Paramagnetic Resonance of Irradiated Sodium Beta-Alumina," this report.

TEMPERATURE-DEPENDENT EFFECTS IN THE RAMAN SCATTERING FROM SODIUM AND SILVER BETA-ALUMINA[1]

J. B. Bates Roger Frech[2]

The Raman spectra of sodium and silver beta-alumina measured at several temperatures have been previously reported.[3,4] With the exception of changes in the band assigned to the attempt mode, the reported spectra surprisingly showed virtually no changes over a temperature range from 4.2 to 900 K. Apparently all of the Raman spectra were recorded using a 90° scattering geometry in which the crystallographic c axis was parallel to the direction of scattered light. We have investigated the temperature-dependent behavior of the Raman scattering from sodium and silver beta-alumina single crystals oriented so that the c axis was perpendicular to the directions of incident and scattered radiation. This allowed us to measure the contribution to the scattering from modes in which the induced electric-dipole moment was parallel to crystallographic c axes. The region between 230 and 50 cm^{-1} in the $a(cc)a'$ Raman spectra of both compounds undergoes a noticeable change with temperature, and the spectral changes observed in this region of Naβ-Al_2O_3 are shown in Fig. 2.15. The most obvious change in these spectra is the decrease in intensity of the band at 163 cm^{-1} with increasing temperature above 12 K accompanied by a noticeable change in the shape of a broad band centered around 200 cm^{-1}. The latter feature appears to narrow with increasing temperature and gradually disappears into the wing of the strong A_{1g} band at 260 cm^{-1}, which broadens with increasing temperature. The bands shown in Fig. 2.15 are evidently due to modes in which the atom displacements are parallel to the c axis, since these bands were not seen in comparable scans with $a(a'a')c$ or $a(a'a)c$ scattering geometries. The appearance of these bands in $a(cc)a'$ but not in $a(a'c)a'$ or in $a(ca)a'$ spectra means that they arise from totally symmetric modes.

A graph of the intensity of the 163-cm^{-1} band of Naβ-Al_2O_3 vs temperature is shown in Fig. 2.16. The data points represent the normalized intensities from four experiments with two crystals. In contrast to the behavior exhibited by the 163-cm^{-1} band, the intensity of the 100-cm^{-1} E_{2g} mode increased linearly with increasing temperature as did the intensity of the A_{1g} mode at ~98 cm^{-1}. The temperature-dependent behavior of the 163-cm^{-1}

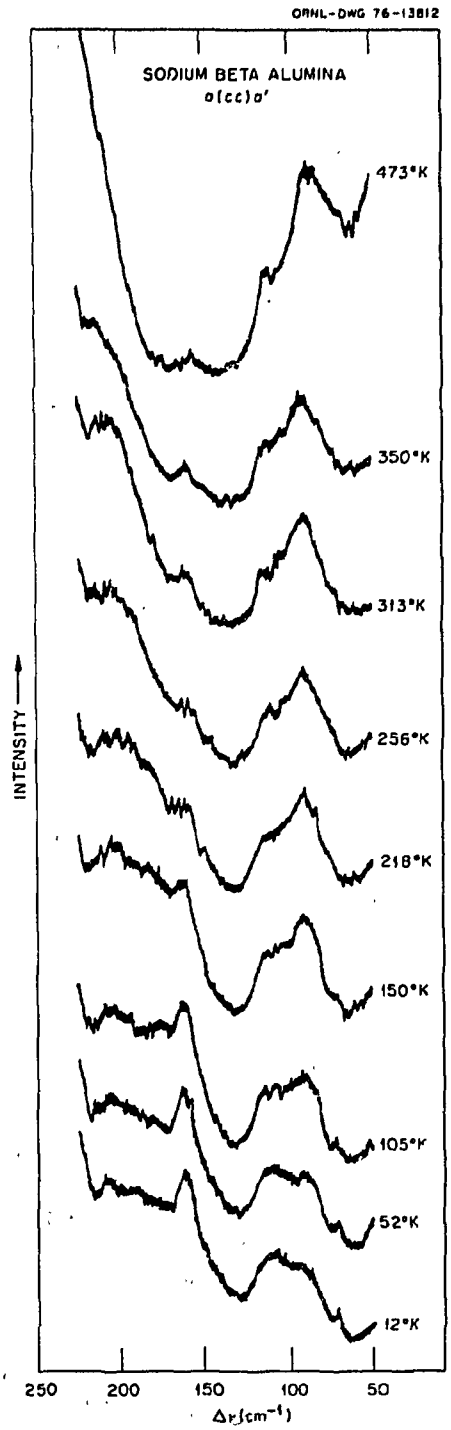

Fig. 2.15. Bands due to temperature-dependent modes in the low-frequency region of the *a(cc)a'* Raman spectra of sodium beta-alumina.

band may reflect an order-disorder phase transition involving a redistribution of Na^+ ions over the available sites. It is interesting to note that behavior

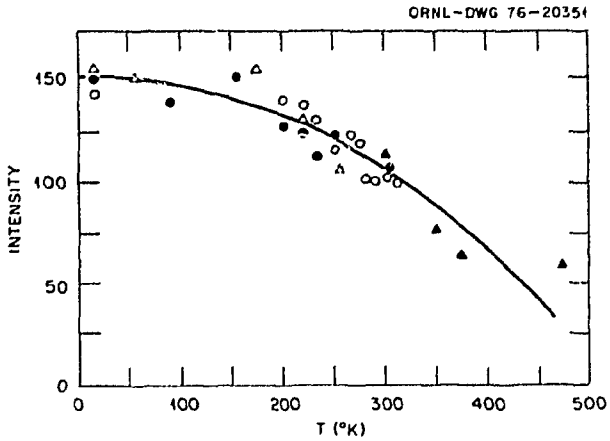

Fig. 2.16. Peak intensities (in arbitrary units) of the 163 cm^{-1} A_{1g} band of sodium beta-alumina plotted as a function of temperature. The open and closed circles and triangles represent data points from different experiments.

comparable with that exhibited by the 163-cm^{-1} band in Naβ-Al_2O_3 was recently seen[5] in the temperature dependence of the peak-to-peak width of the absorption derivative of the ^{23}Na nuclear magnetic resonance (NMR) line in this compound. The changes observed between 120 and 300 K were ascribed to thermally activated jumping of ions among different sites.

---

1. Summary of paper: *Chemical Physics Letters* (in press).
2. ORAU summer faculty participant from the University of Oklahoma, Norman.
3. L. L. Chase, C. H. Hao, and G. D. Mahan, *Solid State Commun.* 18, 401 (1976).
4. C. H. Hao, L. L. Chase, and G. D. Mahan, *Phys. Rev. B* 13, 4306 (1976).
5. W. Bailey et al., *J. Chem. Phys.* 64, 4126 (1976).

SUPERCONDUCTING PROPERTIES OF NIOBIUM IRRADIATED WITH 15-MeV NEUTRONS AT LOW TEMPERATURE[1]

H. R. Kerchner
R. R. Coltman, Jr.
C. E. Klabunde
S. T. Sekula

We have investigated the influence of high-energy-neutron damage on flux line motion in superconducting niobium in the mixed state. This investigation was part of an experimental study of the production and isochronal recovery of high-energy-neutron damage in three metals: copper, platinum, and niobium.[2] The critical

current, flux-flow resistance, and normal-state resistance were measured by using a standard four-terminal technique.

The critical-current density was observed to increase with irradiation and to decrease toward the preirradiation value with isochronal annealing between 4.2 and 360 K. We deduced the elementary, flux-line-pinning force f_p of the high-energy-neutron defect cascades from the data in two ways by using Kramer's model[3] and Labusch's model[4] for flux-line-lattice relaxation. The results for both models are shown in Fig. 2.17.

We also calculated the elementary pinning force of the defect cascades. The interaction between a defect cascade and a flux line, which is dominated by the so-called "$\Delta\kappa$ interaction," is repulsive at short range and attractive at low fields and longer range. For flux densities B near the upper critical field H_{c2}, pinning is dominated by the repulsive interaction, which varies with flux density roughly in proportion to $1 - B/H_{c2}$. At lower flux densities, the attractive interaction rises sharply with decreasing B and dominates flux line pinning.

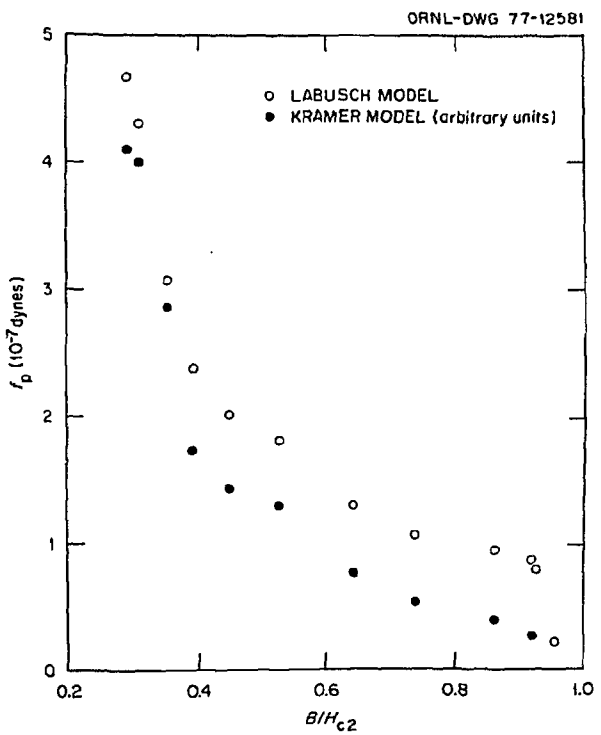

Fig. 2.17. The flux-density dependence of the elementary pinning force of the defect cascades. The elementary pinning force was derived from the critical-current measurements in two ways using two different models of the flux-line-lattice relaxation.

While the field dependence of the pinning force for most types of defects is similar to that of the repulsive interaction, the steep rise in the attractive pinning force at low B is a unique property of low-temperature, high-energy radiation damage. This steep rise in the pinning force is clearly evident in the data shown in Fig. 2.17.

In addition, the low-field ($B < 0.7H_{c2}$) flux-flow resistivity was observed to be unaffected by irradiation or isochronal annealing, while the high-field ($B > 0.7H_{c2}$) flux-flow resistivity varied in proportion to the normal-state resistivity. This result provides direct evidence that the moving flux lines largely avoid the defect cascades. The difference between low-field and high-field behavior arises from the fact that dissipation takes place mainly in the flux line cores at low fields and throughout the sample near H_{c2}.

---

1. Summary of paper: *Journal of Nuclear Materials* (in press).
2. J. B. Roberto et al., "Isochronal Recovery of High-Energy *d*-Be Neutron Damage in Copper, Niobium, and Platinum from 8 to 400 K," this report; J. B. Roberto et al., "Damage Production by High-Energy *d*-Be Neutrons in Copper, Niobium, and Platinum at 4.2 K," this report.
3. E. J. Kramer, *J. Appl. Phys.* **44**, 1360 (1973).
4. R. Labusch, *Cryst. Lattice Defects* 1, 1 (1969).

IRRADIATION AND ANNEALING STUDY OF V_3Ga

T. L. Francavilla[1] D. U. Gubser[1]
B. N. Das[1] R. A. Meussner[1]
S. T. Sekula

We have studied the effect of fast-neutron irradiation ($E > 1$ MeV, at 60°C) on the superconducting properties of V_3Ga at three compositions spanning the *A*15-phase field. Transition temperatures (T_c) of all specimens irradiated in stages to a level of 1.2×10^{19} neutrons/cm^2 show a gradual depression similar to other *A*15 materials; however, annealing studies have revealed some unusual features. Initial annealing studies indicated the possibility of two distinct recovery steps: one occurring at temperatures as low as 200°C, the other occurring at 350 to 450°C. We attribute this low-temperature recovery to radiation-enhanced diffusion. We are currently reexamining these recovery steps in an attempt to evaluate the temperature coefficients for these processes. The lattice parameter has also been

found to increase with irradiation and decrease during annealing.

---

1. U.S. Naval Research Laboratory, Washington, D.C.

NEUTRON-INDUCED DISORDER IN V_3Ga AS REVEALED BY ISOCHRONAL ANNEALING[1]

T. L. Francavilla[2] R. A. Meussner[2]
S. T. Sekula

Fast-neutron irradiation has been found to have a deleterious effect on the superconducting properties of V_3Ga similar to that observed in other $A15$ materials. The recovery of the transition temperature T_c of a V_3Ga sample irradiated with fast neutrons (6×10^{18} neutrons/cm^2, $E > 1$ MeV) was measured after each of a series of isochronal anneals. These results were compared with a similar annealing study of V_3Ga by other workers where disorder was introduced by arc melting and quenching. We have found that the T_c of the irradiated sample recovered at annealing temperatures lower than that required for the unirradiated sample. We attribute this lower recovery temperature to the enhancement of diffusion provided by the defects produced during irradiation.

---

1. Abstract of paper: *Solid State Communications* (in press).
2. U.S. Naval Research Laboratory, Washington, D.C.

EFFECT OF IRRADIATION ON THE CRITICAL CURRENTS OF ALLOY AND COMPOUND SUPERCONDUCTORS

S. T. Sekula

The effects of energetic-particle irradiation on the critical-current density $J_c(H)$ of several superconducting compounds and Nb-Ti alloys have been examined by a number of workers. The irradiations used in the investigations include electrons, fast neutrons, ions, and fission fragments. The results of these studies are reviewed and summarized. In the alloys, changes in $J_c(H)$ on irradiation depend on the metallurgical history of the material and indicate that radiation defects modify the strength of the interaction between the fluxoid array and the sample microstructure. Radiation defects in alloys can also affect $J_c(H)$ through small decreases in T_c, the transition temperature, and increases in ρ, the normal-state resistivity. Irradiations of $A15$ compounds up to moderate fluences (dependent on the type and energy of irradiating particle) lead to decreases in T_c of about 1 K and increases in $J_c(H)$ with dose for most of the samples investigated. This result can be qualitatively understood as resulting from radiation-induced changes in ρ and the pinning force acting on the fluxoids. At higher dose levels, significant depressions of T_c and possibly γ, the electronic specific heat coefficient, lead to drastic reductions in $J_c(H)$. The effect of various energetic particles and irradiation temperature on changes in $J_c(H)$ is examined.

AC PERMEABILITY OF DEFECT-FREE TYPE-II SUPERCONDUCTORS

H. R. Kerchner S. T. Sekula

We have derived the stress-tensor formulation of the theory of the ac permeability of a defect-free type-II superconductor in the mixed state. The stress-tensor formulation corrects the theory based on Maxwell's equations combined with Ohm's law. The correction arises from the energy associated with shearing the flux line lattice. Of particular interest is the case of a cylindrical sample in a large, axial dc magnetic field and a small, parallel ac field. Our previous experimental and theoretical study[1] showed that, while viscous-loss effects clearly dominated the ac response in nearly defect-free samples, there were significant discrepancies between theory and experiment. Although the present study was undertaken in order to understand these discrepancies, the correction we calculated does not account for the observations.

The transport current density in a superconductor in the mixed state is associated with distortions of the flux line lattice. For example, the flux lines bend in a slab in a perpendicular magnetic field, there is a gradient in the flux line spacing in a slab or a cylinder in a parallel field, and both occur in other geometries. The stress tensor for the flux line lattice is related to the strain tensor by three independent elastic moduli, C_{44} (for flux line bending), C_{66} (for shearing in the plane perpendicular to the field), and $C_L = C_{11} - C_{66}$ (for compression), in Voigt's notation.

The stress-tensor formulation of ac flux motion in a cylinder parallel to the ac and dc magnetic fields results in a differential equation that can be

reduced to Bessel's equation. The ac permeability then is related to Bessel functions of complex argument. The permeability has been numerically evaluated and tabulated[2] for several values of the parameter $\alpha = (1 - C_{66}/C_L)/(1 + C_{66}/C_L)$. The result for $\alpha = 1$ ($C_{66} = 0$) is identical to the result obtained previously.[1]

1. J. R. Clem, H. R. Kerchner, and S. T. Sekula, *Phys. Rev. B* 14, 1893 (1976).
2. The numerical computation was done by H. L. Davis.

AC LOSSES IN TYPE-II SUPERCONDUCTORS WITH PINNING DEFECTS

H. R. Kerchner S. T. Sekula

We have continued experimental studies of ac losses in the mixed state of type-II superconductors when flux line motion is limited both by viscous damping and by the interaction between flux lines and defects in the superconducting material. The initial discovery of the failure of existing theory to describe the frequency and ac amplitude dependence of the loss has been reported previously,[1] and it was shown that the failure of the theory is a consequence of the nonlinear relation between the electric field E and the current density J that is characteristic of nearly all superconducting samples. We have investigated quantitatively the effect of the nonlinear $E(J)$ relation on the low-frequency ac response by two types of measurements.

In our studies, a cylindrical or prolate spheroid sample was placed in a large, axial dc magnetic field and a small, parallel, sinusoidal ac field. Using a Hartshorn mutual-inductance bridge balanced with the sample in the Meissner state, we measured the ac voltage waveform, which is proportional to the instantaneous time derivative of the magnetic flux in the sample, and its time integral, which is proportional to the instantaneous flux in the sample. The voltage waveform was measured by using a boxcar integrator, and its integral was measured by using a wideband lock-in amplifier. The voltage waveform for a sample of a Nb-Mo alloy is shown in Fig. 2.18. The sample-out signal is proportional just to the time derivative of the ac applied field. Both the nonlinear response due to flux pinning and the phase shift due to flux flow are evident in the figure. Of particular interest are the phase shift of the zero crossing of the ac voltage waveform (shifted from the peak or valley of the ac applied field) and the remanent ac flux (measured when the ac applied field is zero). The amplitude and frequency dependence of the remanent ac flux were used to calculate $E(J)$ at large E and J in samples with weak pinning. The amplitude and

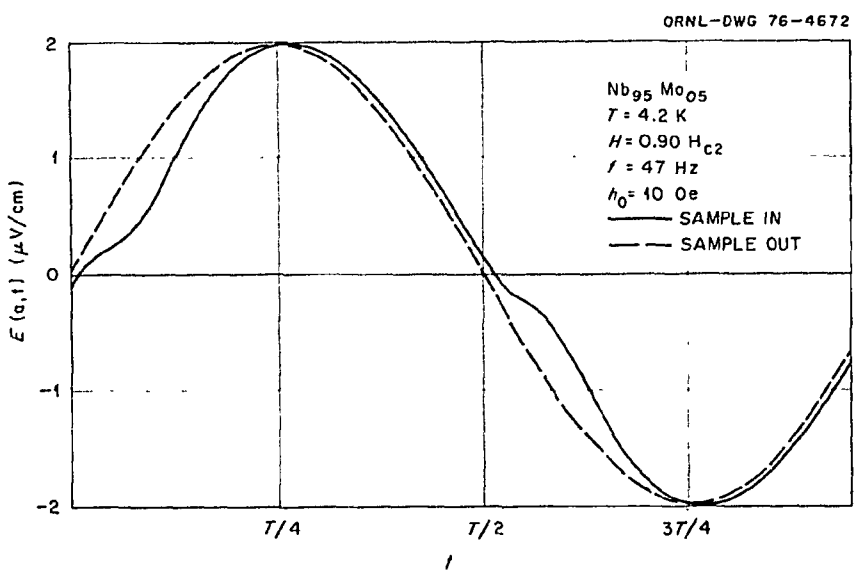

Fig. 2.18. The electric field $E(a, t)$ at the surface of the sample plotted as a function of time t for one cycle of the ac applied field. The electric field is related to the measured voltage simply by a geometrical factor. The sample-out signal is proportional to the time rate of change of the ac applied field.

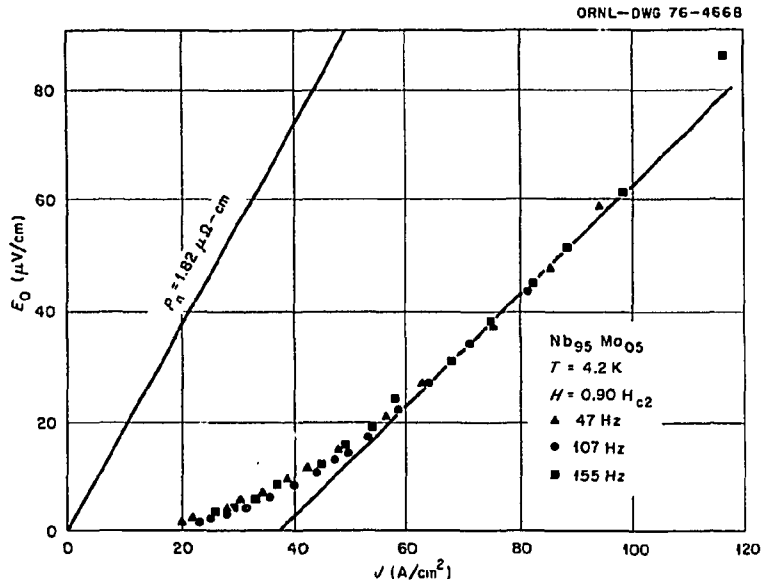

Fig. 2.19. A typical $E(J)$ relation deduced from the amplitude dependence of the remanent ac flux.

frequency dependence of the phase shift of the zero crossing provided information about $E(J)$ at small E in either weakly pinned or strongly pinned samples. At low amplitudes in samples with strong pinning, the phase shift of the zero crossing exhibited several remarkable characteristics. It was independent of frequency at low frequencies, but strongly dependent on amplitude, and it changed drastically if the dc applied field was slowly swept up or down instead of being held constant. All these features are consistent with an exponential $E(J)$ relation, $E = E_0 e^{J/J_0}$. An exponential $E(J)$ relation was deduced previously from logarithmic flux creep observed over times of the order of minutes.[2] The phase shift of the zero crossing was also observed previously,[3] but the relation between the two effects was never understood.

At high amplitudes in samples with weak pinning, the phase shift of the zero crossing was not consistent with an exponential $E(J)$ relation. The additional complexity probably resulted from the fact that the electric field was much larger and that viscous damping of flux line motion was important. In weakly pinned samples, the measurements of the remanent ac flux were more interesting because the linear portion of the $E(J)$ relation could be investigated at high amplitudes. The results of such measurements for the Nb-Mo sample are shown in Fig. 2.19. There the $E(J)$ curve is derived from the amplitude dependence of the remanent ac flux at one frequency.

Results like that of Fig. 2.19 were obtained at several frequencies and dc applied fields in a variety of samples. Curves obtained under the same conditions but at different frequencies consistently showed a small but significant discrepancy. Careful analysis of the data has suggested that the problem lies in our neglect of terms higher than first order in the frequency. Apparently, the nonlinear nature of the $E(J)$ relation causes these terms to contribute more than one expects to the ac response, just as the first-order term contributes more than we originally expected. We plan to measure the $E(J)$ data directly by dc methods and compare the results with remanent ac flux measurements on the same material. We expect that a careful extrapolation of the ac measurements to zero frequency will give the correct $E(J)$ relation.

---

1. H. R. Kerchner and S. T. Sekula, *Solid State Div. Annu. Prog. Rep. Dec. 31, 1975*, ORNL-5135, p. 30.
2. P. W. Anderson and Y. B. Kim, *Rev. Mod. Phys.* 36, 39 (1964).
3. R. W. Rollins, H. Küpfer, and W. Gey, *J. Appl. Phys.* 45, 5392 (1974).

SURFACE PHYSICS AND CATALYSIS

LEED ANALYSIS OF THE COPPER (110) SURFACE

J. R. Noonan H. L. Davis L. H. Jenkins

A low energy electron diffraction (LEED) study of the Cu (110) surface has been initiated. This study has two primary motivations. First, there exists a growing interest in the crystallography of the (110) surfaces of fcc transition and noble metals. This interest has been generated because work by others has shown that such (110) surfaces usually have significant differences from the idealized surfaces which would result if the bulk crystals merely were truncated without any relaxation, dilation, or contraction. Thus since it has not been previously investigated in any detail, a study of the Cu (110) surface could possibly contribute to the general understanding of the (110) surfaces of fcc metals. Our second motivation is eventually to study the adsorption of atomic species (e.g., oxygen or sulfur) on the Cu (110) surface. In order to determine surface positions where such species are adsorbed, it is first absolutely necessary to investigate the crystallography of the clean Cu (110) surface.

Although our study of the Cu (110) surface is still in progress, it is worthwhile to describe some of the preliminary results. To date, experimental LEED intensity profiles have been obtained for the {01}, {10}, {11}, {02}, {20}, and {12} beams, when the incident electron beam is normal to the surface. The Cu(110) sample was prepared using methods previously described[1,2] to produce a surface oriented within 0.5° of the (110). Alignment in the LEED chamber was such that the crystal surface was normal to the electron beam to within 0.1°. The current-energy profiles were collected with a moveable Faraday cup, utilized as a retarding field analyzer and having a 0.5% energy resolution and a 0.002 str (40 mil diam) aperture. With this experimental arrangement, intensity profiles of diffraction beams related by symmetry agreed to better than 12% in absolute intensity and ±0.5 eV in peak position.

The lower curve of Fig. 2.20 illustrates the data collected for the (01) beam. The other curves of Fig. 2.20 are calculated curves, which were obtained using computer codes previously described.[3] The model used in performing the calculations assumed that atoms in the surface layers occupy bulk positions, except that the interlayer spacing between the two top surface layers deviates from the bulk value. Each

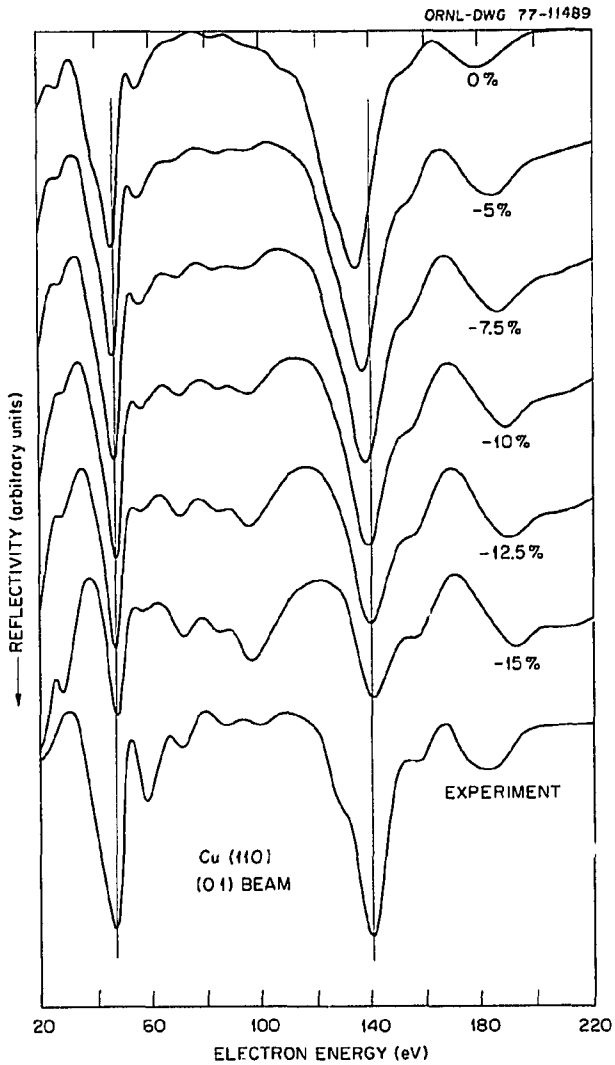

Fig. 2.20. Calculated and experimental LEED current-energy curves for the (01) beam of the copper (110) surface, where the incident electron beam is normal to the surface.

of the calculated curves of Fig. 2.20 is denoted by a percentage figure, which corresponds to the amount of deviation used in the calculations. The energy placements of the two major features of the data at 48 eV and 140 eV are best reproduced by the calculated curve denoted −12.5%. Such reproduction indicates that the interlayer spacing between the top two layers of the Cu (110) surface is probably contracted from the bulk value by an amount 12.5 ± 2.5%. This result is preliminary, and work is in progress to compare calculated and experimental beam intensities for other reflected beams where the incident beam is normal to the surface. Work is also in progress for

cases in which the incident beam is not normal to the surface.

1. L. H. Jenkins, *J. Electrochem. Soc.* 117, 630 (1970).
2. D. M. Zehner, J. R. Noonan, and L. H. Jenkins, *Solid State Commun.* 18, 483 (1976).
3. H. L. Davis, *Solid State Div. Annu. Prog. Rep. Dec. 31, 1975*, ORNL-5135, p. 5.

ANOMALOUS Au (111) SURFACES STUDIED BY LEED, AES, AND OXYGEN CHEMISORPTION[1]

D. M. Zehner J. F. Wendelken

Although the atomic arrangements in the outermost layer of clean Au (100) and (110) surfaces are reordered relative to their ideal intraplanar arrangements in the bulk, previous LEED studies of the Au (111) surface suggest that it exhibits the normal bulklike atomic configuration.[2,3] However, LEED photographs obtained during these previous studies exhibit large areas of intensity at the integral order reflection positions instead of sharp narrow beams.

We have recently completed LEED studies of well-oriented, clean, annealed Au (111) surfaces of both bulk and thin film samples. Instead of a simple (1 × 1) LEED pattern, each integral order beam is surrounded by hexagonal arrays of additional reflections. Although the beam intensities in the LEED pattern obtained from the bulk sample exhibit the threefold rotational symmetry specific to this crystal orientation, those from the thin film specimen exhibit sixfold symmetry as shown in Fig. 2.21. This results from a superposition of threefold symmetric diffraction patterns from adjacent domains, formed during

PHOTO 3505-77

Fig. 2.21. LEED pattern from epitaxially grown Au (111) crystal at a primary beam energy of 54 eV.

epitaxial growth on a mica substrate, which have either *ABC* or *ACB* stacking arrangements. The absence of similar observations of this complex pattern in previous studies on (111)-oriented gold samples may reasonably be attributed to either surface preparation or lack of angular resolution in the electron optics detection system.[2,3]

A careful examination of the LEED pattern reveals that the spatial splitting between the additional reflections, aligned with (110) directions, and the integral order beams is about 4% of the distance between the integral order beams. These results suggest an atomic configuration in the surface region of the (111) different from that in the bulk. Although details of the exact arrangement remain to be determined, a contracted intralayer spacing in the outermost layer may explain these observations and is consistent with previous findings on Au (100) reordered surfaces.

During exposure to oxygen, sample temperatures of 500°C or higher were required to promote chemisorption, and the amount adsorbed for a specific exposure increased with increasing temperature up to the maximum temperature employed, 800°C. The absence of any change in the LEED pattern and the relative size of the oxygen Auger signal suggest that the coverage was much less than a monolayer. This chemisorbed oxygen could be removed by ion bombardment but not by heating to 800°C.

Calcium could be segregated to the surface by heating the sample above 500°C for many hours, and the quantity could be increased with heating time or increased temperature. More oxygen was observed to adsorb for a specific exposure at an elevated temperature when calcium was initially present than on the clean surface. Moreover, the amount of calcium segregating at the surface at a specific temperature increased when the sample was simultaneously exposed to oxygen. Thus, it appears that not only does calcium increase the rate of oxygen adsorption, but it segregates at the surface, bound in a complex that involves adsorbed oxygen.

1. Summary of paper to be published.
2. D. G. Fedak and N. A. Gjostein, *Acta Metall.* 15, 827 (1967).
3. M. A. Chesters and G. A. Somorjai, *Surf. Sci.* 52, 21 (1975).

INTERACTION OF OXYGEN WITH CLEAN REORDERED Au (110)

D. M. Zehner J. F. Wendelken

Previous investigations of Au (100) surfaces have revealed that the atomic arrangement in the outermost reordered layer can be ordered to the normal array by bombarding the reordered surface with an oxygen ion beam.[1] Recently, similar attempts have been made to convert the reordered Au (110) surface to the normal atomic arrangement. The LEED observations indicate that such an arrangement cannot be obtained via oxygen ion bombardment and that the resulting diffuse (1 × 2) pattern suggests surface damage due to the ion bombardment. Auger electron spectroscopy (AES) reveals a small oxygen signal arising from atoms imbedded during the bombarding process. As observed following inert gas ion bombardment, a sharp, reordered (1 × 2) pattern can be obtained subsequent to annealing the oxygen-bombarded surface above 250°C.

Clean Au (110) surfaces have been exposed to oxygen at pressures to 10^{-3} Pa for several hours and over a temperature range from 22 to 500°C. No changes have been observed in the LEED pattern following such exposures, nor has any adsorbed oxygen been detected with AES.

Figure 2.22 illustrates two possible models of the atomic arrangement present on the clean re-

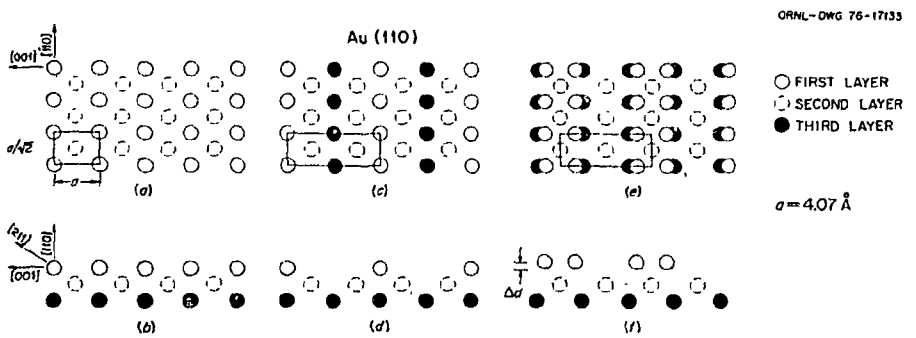

Fig. 2.22. Atomic arrangements in (*a, b*) ideal (110) surface; (*c, d*) missing-row reordered model; and (*e, f*) row-displacement reordered model.

ordered surface.The LEED intensity profiles and positive ion-scattering measurements, which are presently being performed, should provide the data needed to establish the correct geometric configuration in the surface region.

1. D. M. Zehner and J. F. Wendelken, *Solid State Div. Annu. Prog. Rep. Dec. 31, 1975*, ORNL-5135, p. 39.

CHARACTERIZATION OF Au (100) REORDERED AND "NORMAL" SURFACES VIA LEED, AES, AND ELS

J. F. Wendelken D. M. Zehner

Unlike most metals, certain clean crystallographic faces of gold, platinum, and iridium have equilibrium surface geometries at room temperature which are different from the underlying bulk layers. Previously, we determined a procedure for converting the reordered Au (100)-(5 × 20) surface to the "normal" Au (100)-(1 × 1) surface via oxygen ion bombardment.[1] The AES measurements using a retarding field analyzer indicated no oxygen or other impurities present after the oxygen ion bombardment. More sensitive measurements have since been made using a cylindrical mirror analyzer, and these measurements indicate the presence of approximately 0.001 monolayer of oxygen following the bombardment treatment. We have also found that the conversion to the (1 × 1) surface may be effected using either carbon monoxide or nitrogen ion bombardment. As with oxygen ion bombardment, a small quantity of the bombarding ion species is left as an impurity in the surface.

The (1 × 1) surface, which is formed after any of the ion bombardment treatments, is metastable. Heating the (1 × 1) surface to 100°C causes a rapid and complete conversion to the equilibrium (5 × 20) surface structure. The level of impurities following this thermal conversion is essentially unchanged except in the case of nitrogen, which is completely removed by heating. This indicates that the impurities which result from ion bombardment are not sufficient in themselves to stabilize the (1 × 1) structure.

It has recently been shown with ultraviolet photoelectron spectroscopy (UPS) that the electronic structures of Pt (100)[2] and Ir (100)[3] normal surfaces each differed substantially from their reordered counterparts. We have used electron energy loss spectroscopy (ELS) to examine the dependence of the Au (100) electronic structure on the surface geometry. Figure 2.23 shows the ELS data obtained with a primary beam energy of 500 eV using the $[dn(E)/dE]$ mode of data collection. Data in Figs. 2.23*a* and *b* are obtained from a clean (5×20) surface and from a (1 × 1) surface produced by oxygen ion bombardment respectively. Energy losses at 8.5 eV and 14.7 eV are more pronounced for the (1 × 1) surface structure. Figure 2.23*c* shows the loss profile

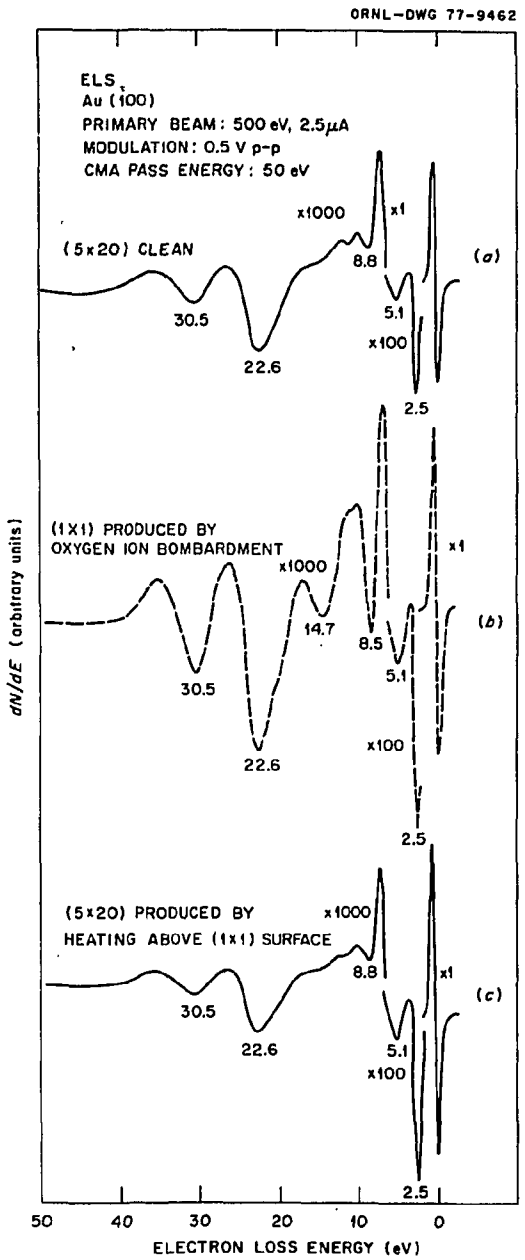

Fig. 2.23. Electron energy loss measurements for (*a*) clean Au (100) – (5 × 20) surface, (*b*) Au (100) – (1 × 1) surface produced by oxygen ion bombardment, and (*c*) Au (100) – (5 × 20) surface produced by heating surface "*b*" above 100°C.

obtained from the (5 × 20) surface following thermal conversion of the oxygen-ion-bombarded (1 × 1) surface and having the same trace contamination of oxygen as that in the (1 × 1) surface. This profile is almost identical to that obtained with the clean (5 × 20) surface; hence, it is the surface structure and not the presence of oxygen that is responsible for the apparent differences in electronic structure. The ELS profiles taken after carbon monoxide or nitrogen ion bombardment show essentially the same results. The unambiguous interpretation of these loss features is very difficult, though we can say that the losses at 8.5 eV and 14.7 eV are associated with the surface. This is consistent with a small but increased sticking coefficient for oxygen which we have observed for the Au (100)-(1 × 1) surface relative to the (5 × 20) surface.

1. D. M. Zehner and J. F. Wendelken, *Solid State Div. Annu. Prog. Rep. Dec. 31, 1975*, ORNL-5135, p. 39; J. F. Wendelken and D. M. Zehner, *Surf. Sci.* (to be published).
2. H. P. Bonzel, C. R. Helms, and S. Kelemen, *Phys. Rev. Lett.* 35, 1237 (1975).
3. T. N. Rhodin and G. Broden, *Surf. Sci.* 60, 466 (1976).

ANGLE-RESOLVED $L_{2,3}VV$ AUGER ELECTRON EMISSION FROM SULFUR ADSORBED ON A Cu (100) SURFACE

J. R. Noonan D. M. Zehner
H. L. Davis L. H. Jenkins

The predominant use of Auger electron spectroscopy has been to determine the elemental constitution of a surface. However, the emitted Auger electron intensity distribution contains significantly more information than element identification. For example, the angle-resolved intensity distribution reflects not only anisotropy of the atomic emission process but also diffraction of the emitted electron from neighboring atoms.[1,2] By examining the angle-resolved Auger electron intensity distribution from an adsorbate on a surface, one could possibly identify site locations of adsorbate atoms. In order to assess the validity of this hypothesis, the angle-resolved $L_{2,3}VV$ Auger electron emission from sulfur adsorbed on a Cu (100) surface is being experimentally measured, and the data are compared with model calculations similar to those applied to angular-dependent Auger spectroscopy (ADAS) of the clean copper surface.[2]

Patterns obtained by LEED show that exposure of a Cu (100) surface to as little as 1.6 mPa·sec of H_2S produces a (2 × 2) sulfur overlayer pattern that corresponds to a quarter-monolayer coverage at saturation. The preliminary data suggest that the copper surface does not reconstruct upon exposure to sulfur, but rather that the sulfur atom is on the surface, possibly in the fourfold hole site. Further comparisons between data and model calculations are being performed, and better adsorption site identification will be established.

1. J. R. Noonan, D. M. Zehner, and L. H. Jenkins, *J. Vac. Sci. Technol.* 13, 183 (1976).
2. H. L. Davis and T. Kaplan, *Solid State Commun.* 19, 595 (1976).

ANGLE-RESOLVED L_3VV AUGER EMISSION SPECTRA FROM Cu (100)[1]

J. R. Noonan D. M. Zehner
L. H. Jenkins

The angle-resolved copper L_3VV (920 eV) Auger electron emission intensity distribution from a clean Cu (100) surface has been measured. The data have been collected as the peak-to-peak intensity of the L_3VV Auger peak in the $N'(\epsilon)$ electron spectrum using a Faraday-cup retarding field analyzer which had a 0.004 str acceptance angle (60 mil aperture). The 920-eV transition intensity distribution shows pronounced structure along several crystallographic directions (Fig. 2.24). The data are plotted as the relative intensity of the Auger peak as a function of polar angle θ along the [001] direction. Interestingly, the major structure aligns with several prominent low-index directions. For example, the peak at $\theta = 0°$ is coincident with the [100], while the peaks at $\theta = 26$ and 45° are quite close to the [210] and [110] crystallographic directions, but the maximum at $\theta =$ 10° cannot be identified with a unique axis because it is near several low-index directions.

Alignment of the angular intensity distribution with prominent crystallographic directions suggests that electron diffraction (i.e., channeling) represents the dominant mechanism in producing the angular intensity distribution of the copper L_3VV Auger transition. Comparison of the data with previously reported angle-resolved data further reinforces this deduction.[2,3] The many similarities between the intensity maxima and the maxima in the angle-resolved photoejected sodium 2*s* electrons and the

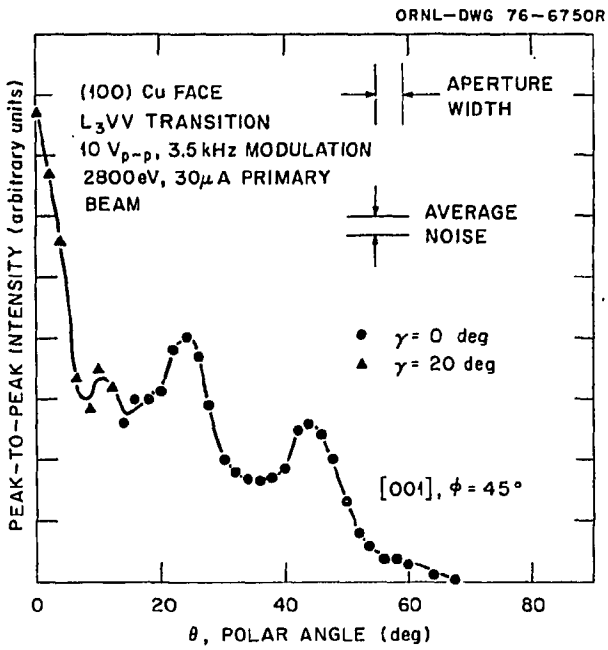

Fig. 2.24. Experimental angular dependence of the L_3VV (920 eV) Auger transition from Cu (100) for $\phi = 45°$, [001], as a function of θ.

sodium KL_2L_2 Auger electrons from NaCl and the photoejected $4f$ electron from gold show that variations in emission character of the high-energy electrons play secondary roles in producing the intensity distribution measured in vacuum. In contrast to previously measured angle-resolved Auger electron emission at low energy (~100 eV) where both initial-state effects and multiple-scattering mechanisms must be considered,[4] the predominant features of angle-resolved higher energy (~1 keV) Auger transitions appear to be explained by electron channeling.

1. Summary of paper: *Physics Letters* (in press).
2. C. S. Fadley and S.A.L. Bergström, *Phys. Lett.* 35A, 375 (1971).
3. K. Siegbahn et al., *Phys. Lett.* 32A, 221 (1970).
4. H. L. Davis and Theodore Kaplan, *Solid State Commun.* 19, 595 (1976).

LINE SHAPE ANALYSIS OF COPPER AUGER SPECTRA

D. M. Zehner J. R. Noonan
H. H. Madden[1]

Information about the Auger process, including details of the matrix elements involved, in principle can be obtained by determining the true Auger transition line shape. Moreover, because of the small mean-free path, the line shape of those Auger transitions in which valence band electrons participate should provide details about the band structure (electronic structure) at the surface of a solid. However, the conventionally measured Auger line shape differs from that of the true line shape because of instrumental resolution limitations, the occurrence of discreet electron-loss events, and the existence of a smoothly varying secondary electron background resulting from higher energy electron cascades within the solid. Recently, we have attempted to obtain true Auger line shapes for several Auger transitions from copper by employing a procedure which provides for the removal of the distorting effects.[2]

The treatment of the measured data proceeds in the following fashion. Because the secondary electron background resulting from higher energy electron cascades is generally smoothly varying in the region of interest, it can be analytically modeled and thus removed. The discreet electron-loss processes are removed by assuming that a reasonable approximation to this loss function can be obtained by measuring the backscattered energy spectrum of an electron beam incident on the sample with an energy near that of the Auger transition of interest. Because both this function and the measured Auger line shape are obtained with the same instrument, the subsequent deconvolution of the two not only removes the loss structure from the line shape but also removes instrumental distortions. The resulting line shape is then assumed to be a good approximation to the true Auger line shape.

The deconvolved line shapes of the three most intense Auger transitions originating in copper are shown in Fig. 2.25. While the highly resolved L_3VV line shape has been obtained previously in photo-excited Auger measurements, the line shapes of both the $M_{2,3}VV$ and M_1VV transitions have not been reported in this form before. A comparison of the L_3VV line shape presented here with those obtained previously shows excellent agreement within the resolution capability of the instrument used, that is, about 0.4%. Since the $M_{2,3}VV$ line shape contains transitions originating in either the M_2 or M_3 core levels, which are split by about 2.5 eV, these separate line shapes overlap each other as seen in Fig. 2.25.

Because all measured transitions involve the participation of two valence band electrons, the widths of the true line shapes should be approximately twice the valence bandwidths as shown in Fig. 2.25. The final state configuration for each

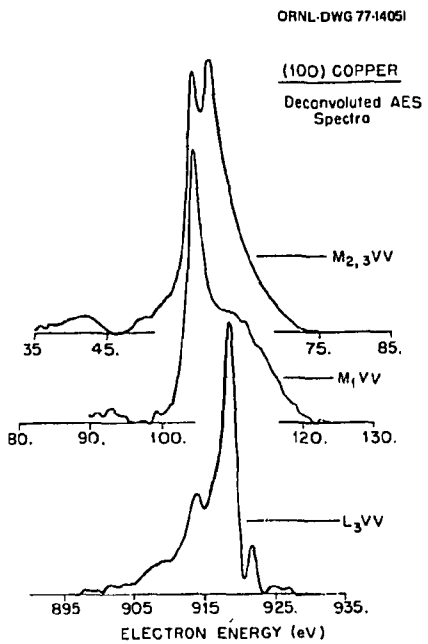

Fig. 2.25. Deconvoluted copper Auger electron line shapes.

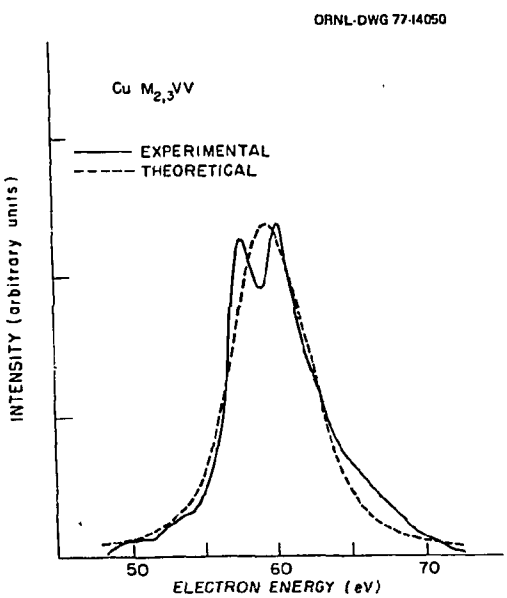

Fig. 2.26. Comparison of copper $M_{2,3}VV$ deconvoluted Auger electron spectrum (solid curve) with calculated line shape (dashed curve).

transition contains two holes in the valence band; thus a simple density-of-states model would suggest that all measured line shapes should be the same. An examination of Fig. 2.25 shows this not to be the case and more importantly reveals sharp, narrow features in each line shape. Previous interpretations of the L_3VV line shape have suggested that the sharp structure is indicative of a quasi-atomic transition in which the two final state holes are localized on the atom, thus exhibiting little solid state effects. The similar sharp features in the $M_{2,3}VV$ and M_1VV line shapes would suggest an analogous interpretation for these spectra.

Supporting evidence for this interpretation comes from an examination of Fig. 2.26, which shows a comparison of the measured $M_{2,3}VV$ line shape with results of a calculation in which the surface band structure and atomic transition matrix elements were employed.[3] While there is some agreement in overall width, the sharp features are not reproduced in the calculated results. This may arise because of the neglect of the two-hole interaction energy in the calculation. Thus it appears that there are some quasi-atomic features in all of the line shapes, and an understanding of this phenomenon is presently being sought.

---

1. Sandia Laboratories, Albuquerque, N.M.
2. H. H. Madden and J. E. Houston, *J. Appl. Phys.* 47, 3071 (1976).
3. P. J. Feibelman and E. J. McGuire, *Physical Review B* (to be published).

HIGH-RESOLUTION ELECTRON ENERGY LOSS SPECTROSCOPY

J. F. Wendelken

A program of high-resolution electron energy loss spectroscopy studies with clean and adsorbate covered metal surfaces has been initiated. In particular, measurements will be made of the vibrational energies of well-ordered adsorbates on single crystal substrates. Such measurements are made by observing the discrete energy losses (50 to 500 meV) that occur when a low-energy (10 to 50 eV) electron beam excites an adsorbate vibrational mode in the process of inelastic diffraction from the surface. Knowledge of these vibrational energies may be used to help determine the adsorbate-substrate bonding geometry.[1] Preparations are under way for a study of the vibrational spectrum of oxygen adsorbed on Cu(110) which will complement the detailed LEED measurements currently in progress on this same system and which will also be analyzed for structural information.

These studies will utilize a high-resolution low-energy electron diffractometer initially built at the

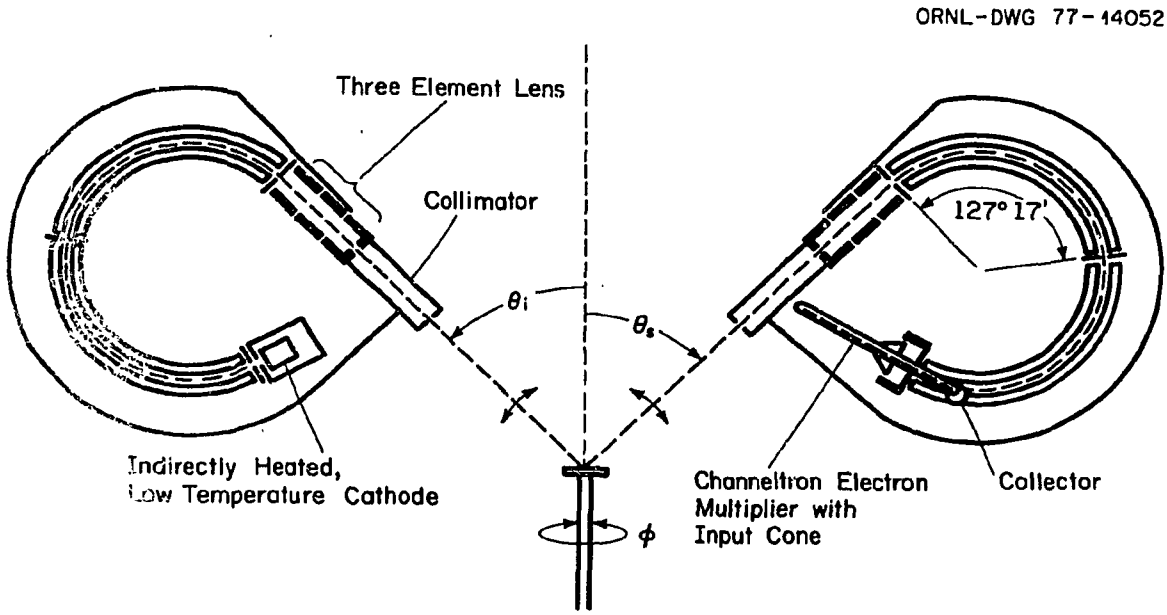

Fig. 2.27. Schematic of high-resolution low-energy electron diffractometer. The monochromator is to the left and the electron energy analyzer is to the right.

University of Illinois[2] and recently modified at ORNL. Figure 2.27 is a schematic drawing of the instrument. Double-pass 127° electrostatic energy selectors are used in both the monochromator and the energy analyzer. With an electron pass energy of about 1.5 eV, a resolution of 30 meV may be obtained. By operating at a constant pass energy, the resolution remains constant and is independent of the electron beam energy (5 to 450 eV), which is controlled through a series of lenses. The angular divergence of the electrons is limited to 1° by collimators on the monochromator and the analyzer. Angular studies are allowed by rotation of the monochromator and the analyzer about a common axis θ and by rotation of the target about a perpendicular axis ϕ. The target may be cooled to 85 K by means of a flexible strap connection to a liquid nitrogen reservoir. To prevent magnetic fields from disturbing the trajectories of the very low-energy electrons used in this system, the system is enclosed in a three-layer magnetic shield which reduces the field to less than 2 mG. The diffractometer with magnetic shielding is contained inside a stainless ultrahigh vacuum system to maintain the clean conditions required for surface studies.

1. S. Andersson, *Solid State Commun.* 21, 75 (1977).
2. J. F. Wendelken and F. M. Propst, *Rev. Sci. Instrum.* 47, 1069 (1976).

SPUTTERING OF NIOBIUM BY ENERGETIC NEUTRONS AND PROTONS: A ROUND-ROBIN EXPERIMENT[1]

R. Behrisch[2]
O. K. Harling[3]
M. T. Thomas[4]
R. L. Brodzinski[4]
L. H. Jenkins
G. J. Smith[5]
J. F. Wendelken
M. J. Saltmarsh[6]
M. Kaminsky[7]
S. K. Das[7]
C. M. Logan[8]
R. Meisenheimer[8]
J. E. Robinson[9]
M. Shimotomai[9]
D. A. Thompson[9]

This paper presents the results of a round-robin neutron-sputtering experiment in which six independent research groups have participated. Targets of cold-rolled niobium prepared by two standard techniques were used by all participants. Three participating groups used (d,t) neutrons of about 14.8 MeV, one group used (d,Be) neutrons produced by 40-MeV deuterons on a thick beryllium target, and two groups used 16-MeV protons in transmission. The emission of micrometer-sized particles was observed by two groups and not observed by the other four. This particle emission was observed by two of the groups who used (d,t) neutrons in their irradiations. Chunk emission was observed for only one of the two standardized target types used in the round robin. The round-robin results support the concept that the neutron-sputtering yield of niobium,

including atomic and chunk emission, has an estimated probable value no larger than 10^{-4} atoms per neutron. However, sputtering yields in the range of 1.4×10^{-5} to less than approximately 2.6×10^{-3} are reported here. The probable value for the sputtering yield was found to be independent of the two target preparations and the method of analysis, whether or not chunks were observed.

---

1. Abstract of paper: *Journal of Applied Physics* (in press).
2. Max-Planck-Institut für Plasmaphysik, Garching, Germany.
3. Massachusetts Institute of Technology, Cambridge, Mass.
4. Battelle Pacific Northwest Laboratories, Richland, Wash.
5. Brookhaven National Laboratory, Upton, Long Island, N.Y.
6. Physics Division, ORNL.
7. Argonne National Laboratory, Argonne, Ill.
8. Lawrence Livermore Laboratory, Livermore, Calif.
9. McMaster University, Hamilton, Ontario, Canada.

DEFECTS AND IMPURITIES IN INSULATING CRYSTALS

INFRARED SPECTRAL PROPERTIES IN TiO_2 OF HYDROGEN, DEUTERIUM, AND TRITIUM[1]

J. B. Bates R. A. Perkins[2]

A defect associated with hydrogen is known to have an important effect on the electrical and mass transport properties of rutile. Key questions regarding the structure of this defect and its interaction with the host lattice remain unanswered, even though several spectroscopic investigations of hydrogen and deuterium in TiO_2 have been reported. The goal of our studies is to develop a model of the hydrogen-associated defect in TiO_2 which is consistent with spectroscopic results and with diffusion data.

The specimens of TiO_2 were disks about 1.5 mm thick cut from large single crystal boules (National Lead Co.). The OH^- content was sufficiently high for the intended study, and the as-received material was used without further treatment with H_2. Samples of TiO_2 containing deuterium or tritium were prepared by heating a disk encapsulated with D_2 or T_2 in a quartz ampoule at about 800 K for several hours, followed by heat treatment in O_2 to restore the transparency of the disk. The infrared spectra were recorded with a Fourier transform (interferometric) spectrometer (Digilab Model FTS-20). The theoretical resolution was 1.0 cm^{-1} for the measurements at 300 K and 0.5 cm^{-1} for the measurements at 77 and 8 K.

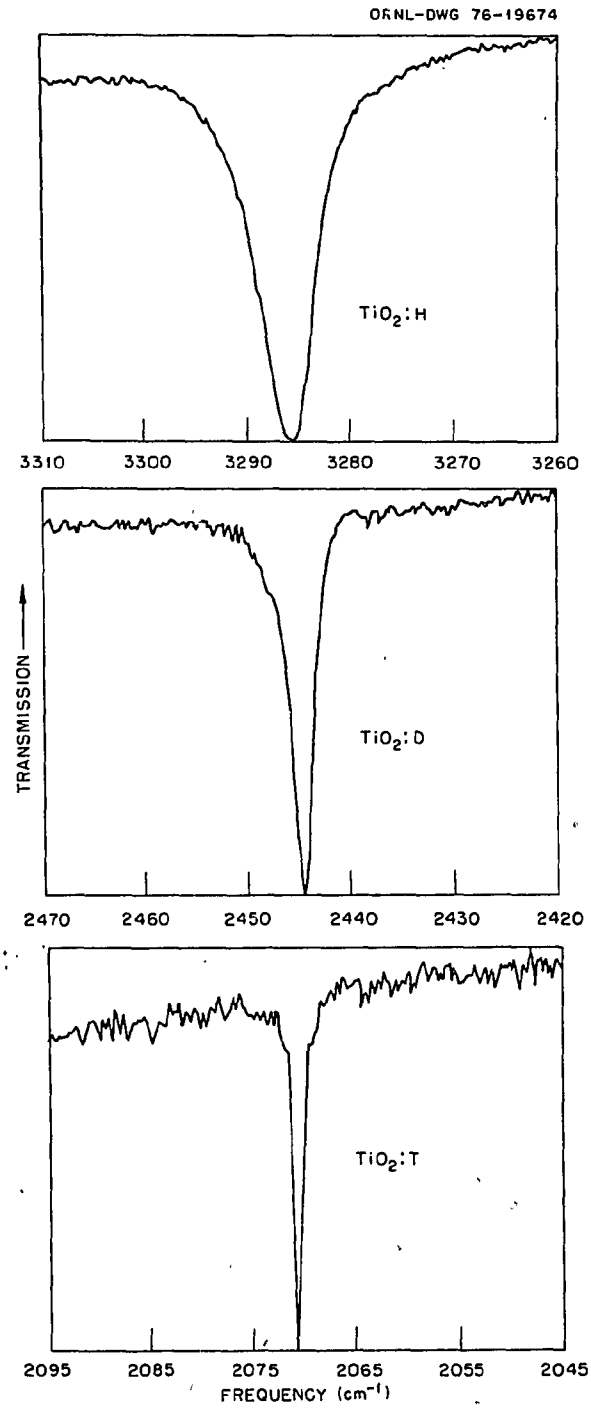

Fig. 2.28. Infrared bands of OH^-, OD^-, and OT^- in TiO_2 recorded at 77 K.

The results obtained from the infrared measurements of the TiO_2:H, TiO_2:D, and TiO_2:T samples are illustrated in Fig. 2.28. In this figure, the spectrum of each sample was expanded to fill the

Table 2.3. Frequencies (ν), bandwidths (δ),[a] and integrated intensities ($\bar{A}$)[b] of the OH^-, OD^- bands in TiO_2:H, TiO_2:D, and TiO_2:T respectively

	TiO_2:H at			TiO_2:D at			TiO_2:T at		
	300 K	77 K	8 K	300 K	77 K	8 K	300 K	77 K	8 K
ν, cm^{-1}	3276	3286	3286.5	2437	2445	2445	2065	2071	2070.5
δ, cm^{-1}	20.0	7.0	7.0	8.0	1.90	2.0	4.5	1.00	1.2
$\bar{A}$, cm^{-1}	1.42	1.51	1.51	2.65	1.89	1.67	0.04	0.11	0.09

[a] Full width at one-half band maximum.
[b] Values of $\int \log [(I_0/I(\nu)]\, d\nu$ where I_0 is the baseline transmission and $I(\nu)$ is the transmission at frequency ν.

ordinate scale. The measured peak frequencies, bandwidths (full width at one-half band maximum), and integrated intensities of the OH^-, OD^-, and OT^- bands at the three temperatures are given in Table 2.3.

The model giving the best agreement with the frequencies listed in Table 2.3 is the anharmonic diatomic oscillator. Based on this model, the energy levels of OT^- are given by

$$G_0^T(\nu) = \omega_0^1 \nu - \omega_0^T x_0^1 \nu^2 ,$$

where ν is the vibrational quantum number. The constants ω_0^T and x_0^T were derived from the OH^- and OD^- frequencies for a given temperature. The calculated OT^- frequencies for the fundamental mode were $G_0^T(1) = 2064\ cm^{-1}$ at 300 K and $G_0^T(1) = 2070\ cm^{-1}$ at 77 and 8 K. These values agree nearly within experimental error with the observed OT^- frequencies listed in Table 2.3.

The integrated band intensities and previously determined[3] absorption coefficients for OH^- and OD^- in TiO_2 were used to calculate the absorption strength per ion for OT^- defined by $a_T = \bar{A}/tn_T$, where t is the sample thickness and n_T is the number of OT^- ions per cubic centimeter. The calculated value, $a_T = 9.24 \times 10^{-18}$ cm, can then be used to determine n_T from a measurement of $\bar{A}$ and t. The TiO_2:T sample measured in this study was found to contain 2.3×10^{16} ions of OT^- per cubic centimeter. Liquid scintillation counting of the same sample found 4.3×10^{16} ions of total tritium per cubic centimeter. The source of the discrepancy between the two values is not certain at present. One can speculate that the total tritium counted includes unreacted T or T_2 in the TiO_2 lattice, so that it is not surprising that n_T determined by this procedure is higher than n_T determined from the infrared data, since the latter is a measure of the concentration of OT^- alone.

The mean square displacement of OH^-, OD^-, and OT^- in TiO_2 has been calculated because these quantities provide a direct measure of the localized motion of the respective ions and their interaction with the surrounding lattice. The quantities calculated from an anharmonic potential are about 14% larger than the quantities derived from the harmonic approximation. The qualitative agreement between the ratios of the mean square displacements and the infrared bandwidths indicates that phonon scattering is an important contribution to the infrared bandwidths. However, the ratios of the widths measured at two temperatures for the same ion suggest that decay of the local-mode vibrational excitation into multiphonons of the host lattice (perhaps a decay into a phonon continuum) is predominantly responsible for the bandwidths.

1. Summary of paper: *Physical Review* (in press).
2. Metals and Ceramics Division, ORNL.
3. O. W. Johnson, J. DeFord, and J. W. Shaner, *J. Appl. Phys.* 44, 3008 (1973).

V^- AND V^0 DEFECTS IN SrO[1]

J. Rubio O.[2] Y. Chen
H. T. Tohver[3] M. M. Abraham

Positive-ion vacancies in the alkaline-earth oxides, both intrinsic and impurity compensated, have been of immense interest since their identification many years ago.[4] Recently, some fundamental aspects of the formation mechanism for the intrinsic V^- and V^0 defects (positive-ion vacancy with one and two trapped holes, respectively) in MgO have been elucidated.[5,6] While the paramagnetic V^- center has been identified unequivocally in MgO and CaO,[5-7] its identity in SrO has been questionable, since

centers with different parameters have been proposed as the V^- center. It has been conclusively shown that, for MgO, the production of V^- centers depends on the presence of hydrogen in the crystal.[5,6] Assuming a similar dependence in SrO, crystals were grown with intentional hydrogen doping. (The same technique has been used successfully to produce V^- centers in CaO.[7])

The V^- and V^0 defects were detected after a short gamma irradiation at 77 K in hydrogenated SrO crystals that had been previously irradiated with high doses of either neutrons, electrons, or gamma rays. Electron-paramagnetic-resonance (EPR) measurements showed that the V^- center exhibits <100> axial symmetry at 77 K, characterized by $g_\parallel = 2.0013(2)$ and $g_\perp = 2.0705(2)$. At 270 K, the spectrum consists of a single, thermally averaged isotropic line at $g = 2.047(1)$. An extensive ENDOR search at 4.2 K revealed no charge-compensating impurities associated with this center. The V^0 center also displays (100) axial symmetry at 77 K with the following parameters: $S = 1$, $g_\parallel = 2.0012(2)$, $g_\perp = 2.0748(2)$, and $D = 127.05(5) \times 10^{-4}$ cm^{-1}. The absence of V^0 signals at 4.2 K established that the $S = 1$ triplet state is an excited state. At about 210 K, the V^0 centers begin to decay into the more stable V^- center (Fig. 2.29). The latter has a room-temperature half-life of about 25 min.

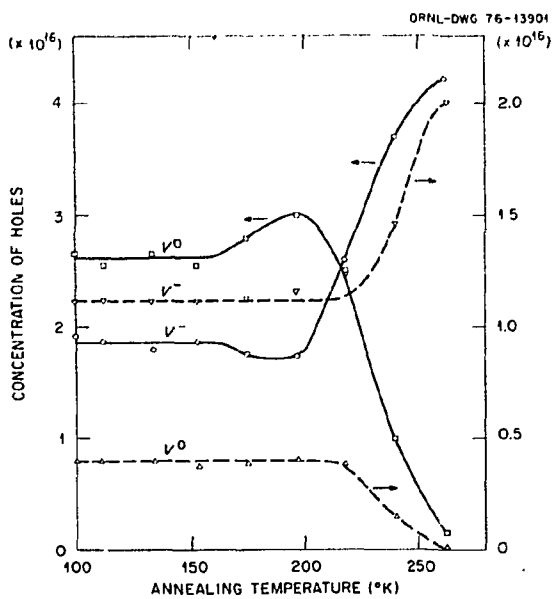

Fig. 2.29. Concentration of trapped-hole centers in SrO as a function of annealing temperature following gamma irradiation at 77 K. The solid line represents a crystal previously irradiated with ^{137}Cs gamma rays at room temperature to about 9×10^8 R. The dashed line represents a crystal previously irradiated with about 1.4×10^{18} neutrons/cm^2.

Our identification of the V^- center in SrO is supported by the motional averaging of the EPR spectra at high temperatures and by the failure of ENDOR to detect any associated magnetic impurities. The production of the V^0 center and its observed decay into the V^- center lend further credence to this identification. Of considerable importance is the fact that we succeeded in producing the V^- center in SrO only in crystals intentionally doped with hydrogen. This was also true in CaO.[6] It was demonstrated previously[5,6] that in MgO the V^-_{OH} center, described by the configuration OH^- — (Mg vacancy) — O^{2-}, is a necessary precursor of the V^- center. We suggest that the same formation mechanism is true in CaO and SrO.

1. Summary of paper: *Phys. Rev. B* **14**, 5466 (1976).
2. Graduate student from Universidad Nacional Autonoma de Mexico, Mexico, D.F.
3. On leave from the University of Alabama, Birmingham.
4. J. E. Wertz et al., *Discuss. Faraday Soc.* **28**, 136 (1959).
5. Y. Chen et al., *Phys. Rev. B* **11**, 881 (1975).
6. Y. Chen and M. M. Abraham, *New Phys.* **15**, 47 (1975).
7. M. M. Abraham et al., *Solid State Commun.* **16**, 1209 (1975) and references cited therein.

DEFECTS IN HYDROGENATED SrO[1]

M. M. Abraham Y. Chen J. Rubio O.[2]

The paramagnetic V_{OH} and V_F defects generated by gamma-irradiation at 77 K have been observed in hydrogenated SrO crystals. At low temperature, EPR and ENDOR measurements were performed to identify the impurity nucleus associated with these defects. In both cases, the defect is axially symmetric about a crystalline <100> axis. An analysis of the anisotropic hyperfine coupling constants of these centers in MgO, CaO, and SrO shows that there is an approximate linear dependence between the distance from the trapped hole (oxygen-fluorine for the V_F and oxygen-oxygen for the V_{OH}) and the crystal lattice parameter. A complex structure in the vicinity of $g \approx 2$, probably due to aggregate defects, was shown to be associated with hydrogen.

1. Summary of paper: *Phys. Rev. B* **14**, 2603 (1976).
2. Graduate student from Universidad Nacional Autonoma de Mexico, Mexico D.F.

ENDOR OF V_{OD} DEFECTS IN SrO

J. L. Boldu[1] Y. Chen
H. J. Stapleton[2] M. M. Abraham

Single crystals of SrO doped with deuterium were grown by the submerged arc fusion technique. The V_{OD} center was produced by gamma-irradiation at 77 K, and its identity was determined by EPR and ENDOR measurements. The angular variation of the deuterium ENDOR spectrum (Fig. 2.30) illustrates the characteristic <100> axial symmetry of these defects, and the spectrum was fit with the following spin Hamiltonian parameters: $g_{\parallel} = 2.0013(2)$, $g_{\perp} = 2.0751(2)$, $A_{\parallel} = +0.396(2)$ MHz, $A_{\perp} = -0.195(2)$ MHz, and $P = +0.158$ MHz. From the hyperfine parameters, a value of 5.08 Å for the OD^-—Sr vacancy—O^- distance in this linear defect can be computed. Since the normal oxygen spacing in SrO is 5.16 Å, this implies that an inward relaxation of the oxygens occurs on formation of the defect. An inward relaxation is contrary to all previously observed cases of V_{OH} and V_{OD} defect formation in the alkaline-earth oxides, where outward distortions from the normal lattice spacings occur.

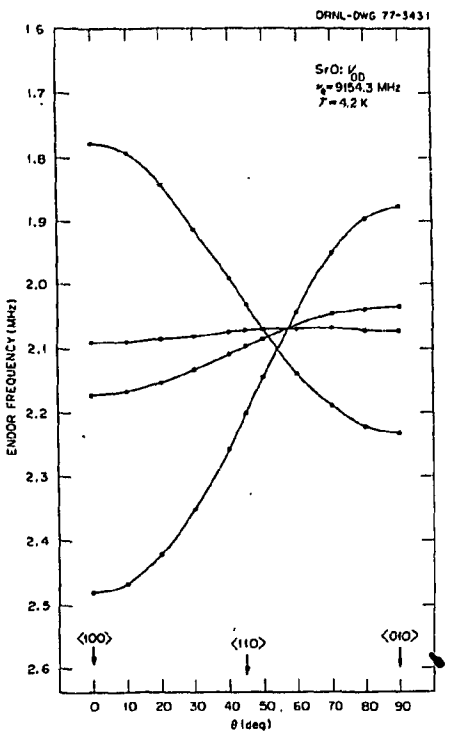

Fig. 2.30. Angular variation in the {100} plane of the ENDOR for the SrO:V_{OD} center.

1. Graduate student from Universidad Nacional Autonoma de Mexico, Mexico D.F.
2. On leave from the University of Illinois, Urbana.

RAMAN SCATTERING FROM *F* CENTERS IN CaO

J. B. Bates R. F. Wood

First-order Raman scattering is formally forbidden in crystals with the rock-salt structure, such as the alkaline-earth oxides. However, the presence of substitutional impurities or defects destroys the translational symmetry, and first-order scattering from modes involving displacements of the ions of the host lattice in the vicinity of the defect can be observed. The *F* center in CaO consists of two electrons trapped at an O^{2-} ion vacancy. The optical properties and electronic structure of this defect have been well characterized in previous experimental[1-3] and theoretical studies.[4,5] The absorption band is centered at 3.1 eV and has a half-width of approximately 0.5 eV; it arises from an allowed transition, $^1A_{1g} \rightarrow {}^1T_{1u}$.

Raman spectra of additively colored CaO crystals containing *F* centers were recorded at 10 K using exciting lines at 457.9, 488.0, and 514.5 nm. The relative intensities of the spectral features and especially sharp structure at 330 and 315 cm^{-1} are dependent on the wavelength of the exciting line. This dependence may arise from a resonance Raman effect, since the higher-energy exciting lines fall well within the broad optical band of the $^1A_{1g} \rightarrow {}^1T_{1u}$ transition. Although the 514.5-nm line is within the wings of the optical band, the spectra obtained with this line are in agreement with the calculated spectra, which do not include resonance.

Theoretical calculations for the off-resonance case were carried out using methods described elsewhere.[6] The perfect crystal eigenfrequencies and eigenvectors were generated using the shell model data of Saunderson and Peckham.[7] Reasonably good agreement with the experimental data was achieved with the various symmetry projections of the perfect crystal density of states, thus suggesting that there are only small force constant changes when the *F* center replaces an O^{2-} ion. The calculations showed that it is

necessary to include polarizability derivatives for both first (Ca^{2+}) and second (O^{2-}) neighbor ions of the defect in order to fit the experimental data at all frequencies.

1. W. C. Ward and E. B. Hensley, *Phys. Rev.* 175, 1230 (1968).
2. B. Henderson, Y. Chen, and W. A. Sibley, *Phys. Rev. B* 6, 4060 (1972).
3. J. B. Bates and R. F. Wood, *Phys. Lett.* 49A, 389 (1974); *Solid State Commun.* 17, 201 (1975).
4. R. F. Wood and T. M. Wilson, *Solid State Commun.* 16, 545 (1975).
5. R. F. Wood and T. M. Wilson, *Phys. Rev. B* 15, 3700 (1977).
6. R. F. Wood, p. 119 in *Methods in Computational Physics*, vol. 15, ed. by Gideon Gilat, Academic Press, New York, 1976; see also R. F. Wood and Mark Mostoller, "First-Order, Induced Raman Scattering from Impurities," this report.
7. D. H. Saunderson and G. E. Peckham, *J. Phys. C* 4, 2009 (1971).

V_K CENTERS IN $RbCaF_3$: LATTICE DISTORTION IN THE TETRAGONAL PHASE[1]

L. E. Halliburton[2] E. Sonder

Intrinsic V_K centers have been produced in single-domain $RbCaF_3$ crystals by electron irradiation at 77 K. The twisting of the CaF_6 octahedra about the tetragonal axis as a result of the 196 K phase change is readily detected in the V_K center EPR spectra. Analysis of these spectra required dividing the six distinct V_K center sites on a given octahedron into two classes and determining the spin Hamiltonian parameters independently for each class.

1. Summary of paper: *Solid State Commun.* 21, 445 (1977).
2. Oklahoma State University, Stillwater.

RADIATION-PRODUCED DEFECTS IN $NaMgF_3$ AND $RbCaF_3$ STUDIED BY OPTICAL ABSORPTION[1]

J. R. Seretlo[2] J. J. Martin[3] E. Sonder

Optical-absorption bands produced by electron irradiation of the compounds $NaMgF_3$ and $RbCaF_3$ were measured as a function of radiation dose, dose rate, and temperature. The band positions, growth rates, and stabilities were compared with corresponding absorptions in alkali halides and $KMgF_3$, permitting the bands observed in $NaMgF_3$ to be attributed, respectively, to self-trapped holes, *F*-type centers, or interstitial defects. The results for $RbCaF_3$ were not as closely analogous with the behavior of alkali halides. Nevertheless the results for both compounds clearly showed that defect production by a radiolysis mechanism was taking place. Since $NaMgF_3$ is orthorhombic and $RbCaF_3$ changes from cubic to tetragonal as the temperature is lowered below 198 K and since their radiation behavior exhibited no effect whatsoever due to these structural differences, the results imply that a replacement collision along close-packed <110> halide rows, an occurrence that has long been assumed to be necessary for radiolysis, may not in fact be necessary for defect production.

1. Summary of paper: *Phys. Rev. B* 14, 5404 (1976).
2. Fulbright Hayes Scholar from University of Fort Hare, South Africa.
3. Oklahoma State University, Stillwater.

CHARGE TRAPPING AND DIELECTRIC BREAKDOWN IN LEAD SILICATE GLASSES[1]

R. A. Weeks D. L. Kinser[2] J. M. Lee[2]

When irradiated with beams of energetic electrons or gamma rays, many insulating glasses and plastics exhibit a spontaneous electrical discharge producing permanent patterns in the materials (Lichtenberg figures). In the case of inorganic glasses, this effect is neither observed in pure silicate, germanate, or phosphate glasses nor in their crystalline forms, and it has only been reported in mixed-oxide glasses with low alkali content. In a series of lead silicate glasses of composition $(PbO)_x(SiO_2)_{(1-x)}$, the effect is observed only for compositions where $0 < x \leq 0.40$. Electron microscopy of these glasses confirms the existence of microphase separation in the range $0.2 \leq x \leq 0.5$. Changes in electrical properties are related to these structural changes in the glasses.

1. Summary of paper: p. 266 in *The Physics of Non-Crystalline Solids*, ed. by G. H. Frischat, Trans. Tech. Publ., Aldermannsdorf, Switzerland, 1977.
2. Vanderbilt University, Nashville, Tenn.

TEMPERATURE-DEPENDENT EFFECTS IN RESONANCE RAMAN SCATTERING FROM O_3^- IONS IN SODIUM CHLORATE[1]

J. B. Bates

The ozonide ion, O_3^-, is produced in alkali-metal chlorates by gamma irradiation at ambient temperature. Resonance Raman scattering from the symmetric stretching mode, ν_1, and its overtones, $n\nu_1$, of O_3^- in $KClO_3$ and $NaClO_3$ was reported earlier.[2] In a recent study[3] of the metastable oxygen center, O_2^*, in gamma-irradiated $NaClO_3$, it was proposed that the first overtone of O_2^*, $2\nu_1$, and a component of $3\nu_1$ of O_3^- are accidentally degenerate, giving rise to the band at 3057 cm^{-1}. The temperature dependence of resonance Raman scattering from O_2^* and O_3^- in $NaClO_3$ was investigated in an attempt to determine the relative contributions from these modes to the scattering at 3057 cm^{-1}. It has been observed in these studies that, for one type of O_3^- ion, the scattering intensity of $n\nu_1$ ($n \geq 2$) increases dramatically with increasing temperature.

Raman spectra of irradiated $NaClO_3$ single crystals were recorded in the $n\nu_1$ ($n \geq 2$) overtone regions of O_3^-. The LO component of the host lattice coincides with ν_1, precluding direct observation of this mode. Measurements were made at sample temperatures from 20 to 100 K using laser exciting lines at $\lambda_0 = 457.9$ and at $\lambda_0 = 488.0$ nm. Temperature-dependent measurements were also made in the 1500 to 1700 cm^{-1} region, which includes the fundamental of O_2^*. Sample temperatures, denoted by $T_{s.a.}$, were determined from the Stokes:anti-Stokes scattering intensity ratio for the 140 cm^{-1} A phonon of the $NaClO_3$ lattice. Depending on the sample, $T_{s.a.}$ was 5 to 15 K higher than the temperature indicated by a sensor located near the sample. The effectively higher sample temperature is due to absorption of the incident laser beam by the color centers in the irradiated crystal and to radiation-induced microscopic fractures, which inhibit heat conduction from the illuminated portion of the crystal to the cold finger. The incident laser power was kept at 90 mW or lower during all measurements to minimize this heating effect.

Examples of the Raman bands observed in the region of $2\nu_1$, $3\nu_1$, $4\nu_1$, and $5\nu_1$ at two temperatures are shown in Fig. 2.31. The vertical bars marked R represent the peak heights ($\times 10^{-2}$) of the 936 cm^{-1} band of the ν_1 mode of ClO_3^-, which is used as an internal intensity standard. With the exception of $2\nu_1$, two components are clearly distinguishable in the overtone regions, and a third component is evident in the $4\nu_1$ and $5\nu_1$ regions (and higher overtone regions not shown) at 20 K. As the sample temperature is increased, the intensities of the lowest frequency $n\nu_1$ components increase rapidly. The increase in intensity of $2\nu_1$ is accompanied by a shift from 2055 to 2050 cm^{-1}, indicating that the lower

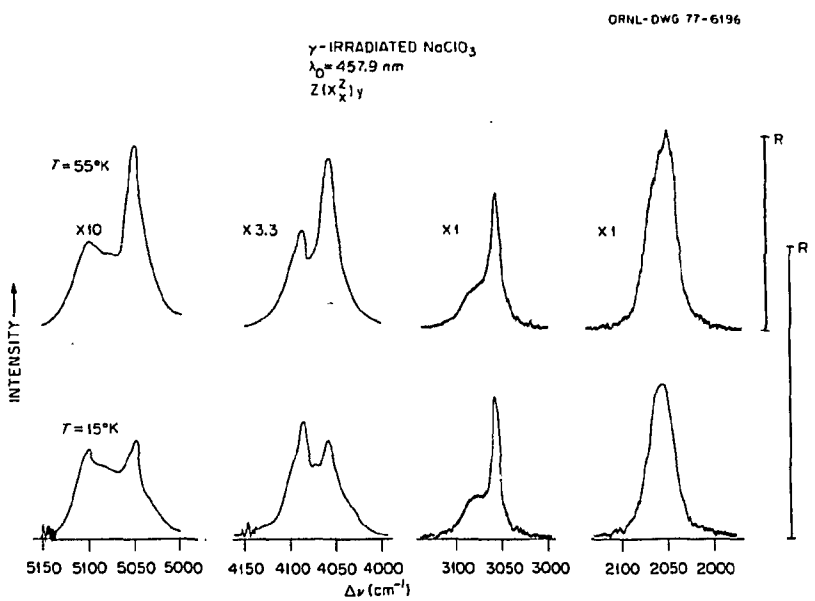

Fig. 2.31. Resonance Raman spectra in the region of $2\nu_1$, $3\nu_1$, $4\nu_1$, and $5\nu_1$ of O_3^- in gamma-irradiated $NaClO_3$. The vertical bars R represent the peak height of the 936 cm^{-1} internal mode of $NaClO_3$.

frequency component of the overlapping doublet (or triplet) becomes dominant at higher temperatures.

Graphs of peak intensity normalized to the internal standard vs sample temperature using 457.9 nm excitation are shown in Fig. 2.32. The 1544 cm^{-1} curve represents the temperature response of the O_2^* fundamental, and the 3057 cm^{-1} curve represents the combined response of 2ν of O_2^* and $3\nu_1$ of O_3^-. The behavior displayed by these curves and that of $2\nu_1$ (2050 cm^{-1}) confirms that 2ν and $3\nu_1$ are accidentally degenerate and that a determination of the fractional contribution to the intensity from both sources can be made from these data. The intensity of a weak band at 1645 cm^{-1} was also found to increase with increasing temperature. The origin of this band is uncertain, but it could be caused by the first overtone of the bending mode of O_3^-, $2\nu_2$, since ν_2 is known to be weakly coupled to the $^2B_1 \rightarrow {}^2A_2$ electronic transition.

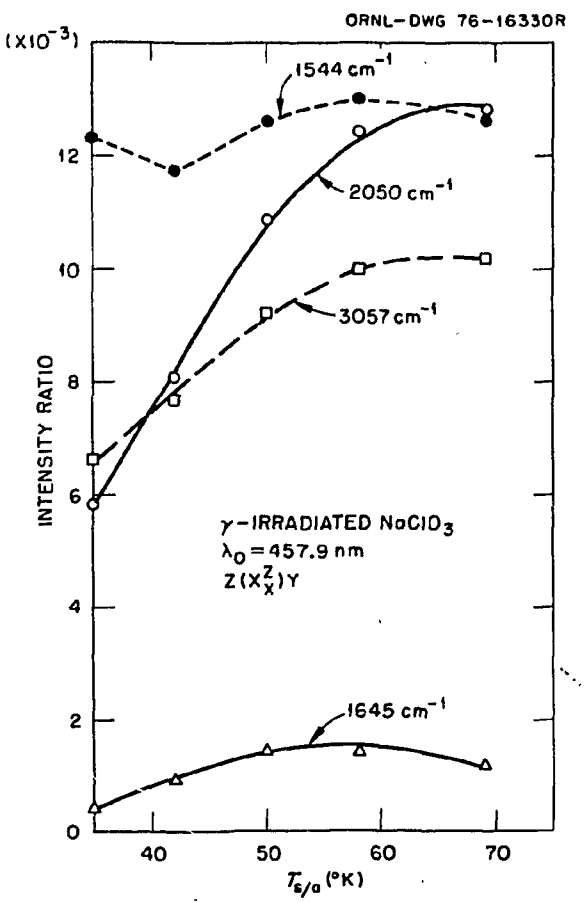

Fig. 2.32. Graphs of the intensity of Raman bands normalized to the internal standard vs sample temperature determined from Stokes:anti-Stokes scattering ratio.

The observed increase in the intensity of $2\nu_1$ by more than a factor of 2 as the sample temperature changed from 35 to 65 K has been interpreted semiquantitatively by using a recent theoretical development in the effects of line broadening on resonance Raman scattering.[4] Using the displaced oscillator model and the Condon approximation, an expression for the Raman scattering intensity for $2\nu_1$ of O_3^-, which included contributions from intramolecular broadening and damping from molecule-lattice interactions, was derived from this theory. It was found that the observed relative intensity changes with temperature for 457.9 and 488.0 nm excitation could be simulated by changing the relative values of the two damping factors while maintaining their sum constant. The sum of the two damping factors was fixed by fitting the calculated $^2B_1 \rightarrow {}^2A_2$ band to the observed optical band[2] of O_3^-.

1. Summary of paper: *Physical Review* (in press).
2. J. B. Bates and J. C. Pigg, *J. Chem. Phys.* 62, 4227 (1975).
3. J. B. Bates and H. D. Stidham, *J. Chem. Phys.* 65, 3901 (1976).
4. A. P. Penner and W. Siebrand, *Chem. Phys. Lett.* 39, 11 (1976).

INVESTIGATIONS OF DIVALENT EINSTEINIUM-253 IN $SrCl_2$ and BaF_2 BY ELECTRON PARAMAGNETIC RESONANCE[1]

L. A. Boatner[2] C. B. Finch[4]
R. W. Reynolds[3] M. M. Abraham

The EPR spectrum of $^{253}Es^{2+}$ ($5f^{11}$ electronic configuration) has been observed in the cubic single-crystal hosts BaF_2 and $SrCl_2$. The spectrum obtained at about 24 GHz and at a temperature of 4.2 K exhibited a well-resolved eight-line hyperfine pattern ($I = {}^7/_2$) for $^{253}Es^{2+}$ in both host crystals, as illustrated in Fig. 2.33. The magnetic field positions of the observed transitions were independent of the magnetic field orientation, but line width anisotropies were present. The EPR spectrum of $^{253}Es^{2+}$ was described by the spin Hamiltonian $H = g\mu_B \mathbf{H}\cdot\mathbf{S}' + A\mathbf{I}\cdot\mathbf{S}'$, with $S' = {}^1/_2$, $I = {}^7/_2$; $g = 5.825(6)$ and $A = 0.1218(3)$ cm^{-1} for the BaF_2 host; $g = 6.658(3)$ and $A = 0.1382(2)$ cm^{-1} for $SrCl_2$. The significant difference between the measured g values for the two hosts indicates that the Es^{2+} ground state is a Γ_6 doublet in BaF_2 and a Γ_7 doublet in $SrCl_2$. Although a similar change in ground states between BaF_2 and $SrCl_2$ has

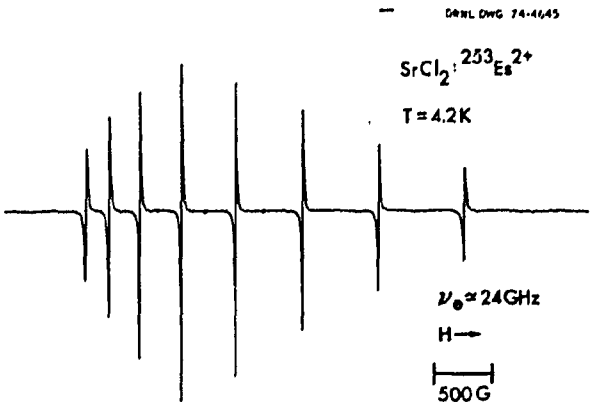

Fig. 2.33. EPR spectrum of $^{253}Es^{2+}$ in a $SrCl_2$ single crystal at a frequency of 24 GHz and a magnetic field orientation H ∥ <100>. The spectrum is shown as a first derivative of absorption. The eight-line hyperfine pattern is due to the $I = 7/2$ nuclear spin of ^{253}Es.

been observed for the rare earth analog of Es^{2+} (i.e., Ho^{2+} with a $4f^{11}$ electronic configuration), a corresponding effect is not necessarily expected for Es^{2+} in view of the known importance of intermediate-coupling effects in the actinide series. The observation of such a correspondence provides an additional example of the increasing "rare-earth-like" behavior of the actinides with increasing atomic number.

---

1. Summary of paper: *Phys. Rev. B* 13, 953 (1976).
2. Ecole Polytechnique Fédérale de Lausanne, Lausanne, Switzerland.
3. General Research Corporation, Huntsville, Ala.
4. Metals and Ceramics Division, ORNL.

PHOTOVOLTAIC CONVERSION OF SOLAR ENERGY

ELECTRICAL PROPERTIES STUDIES OF NEUTRON-TRANSMUTATION-DOPED SILICON

R. T. Young J. W. Cleland R. F. Wood

We have used Hall coefficient and van der Pauw techniques to determine the resistivity, carrier concentration, and mobility of neutron-transmutation-doped (NTD) silicon. Minority carrier lifetime (MCL) was measured by the method of photoconductive decay (PCD). To study the lattice defects introduced by thermal neutrons, samples were irradiated in the thermal neutron facility (D_2O tank) of the Bulk Shielding Reactor (BSR) in a locale where the total thermal neutron fluence was about 10^4 times that of the fast-neutron (>1 MeV) fluence so the separate effect of fast neutrons can be neglected. The rate of removal of conduction electrons per thermal neutron absorption at reactor ambient temperature (≤40°C), as determined by Hall coefficient measurements at −196°C, was about 5 cm^{-1}, which corresponds to the displacement of approximately 4–5 lattice atoms per thermal neutron absorption. Subsequent isochronal annealing experiments showed the presence of distinct annealing stages at about 100 and 300°C and a complete recovery of the initial carrier concentration at about 400°C. This annealing behavior is very similar to that observed for electron or gamma-ray-irradiated silicon and strongly suggests that the same point defects, that is, Si-*E* and -*A* centers and divacancies, are dominant.

The lattice damage introduced by fast neutrons (>1 MeV) is much more complex and is a function of the total fast-neutron fluence. Below a fast-neutron fluence of about 5×10^{18} neutrons/cm^2, the isochronal annealing results indicate that the silicon remains *p*-type after irradiation and annealing to 450°C, that conversion to *n*-type occurs at 500–600°C, and that full recovery of the donor concentration in NTD silicon requires annealing up to 750°C. Above fluences of about 5×10^{18} neutrons/cm^2, the isochronal annealing results are different in that the silicon remains essentially intrinsic, with slightly *n*-type conduction and low carrier mobility, below approximately 600°C. Both the free-carrier concentration and electron mobility increase very rapidly on annealing above 600°C, and again full recovery requires annealing up to 750°C.

Temperature-dependent Hall coefficient measurements were made on selected samples to study the complex annealing behavior of fast-neutron-induced lattice damage and to determine the thermal activation energy of the majority carrier traps. Preliminary results indicate the presence of at least two deep acceptor levels, a deep donor level, and a shallow acceptor level that is formed during the annealing process. Because of the inaccuracy of the Hall effect measurement in determining the deep energy levels, the transient capacitance technique is currently being used.

Minority carrier lifetime measurements, as obtained by the PCD technique, indicate that recovery of the MCL is achieved after the deep acceptor and donor levels are removed by annealing. Samples irradiated to introduce $\leq 10^{15}$ phosphorus atoms per

cm^3 in a reactor locale with a large (>1000) thermal- to fast-neutron ratio showed complete recovery of the MCL after annealing for 2 hr at 600°C, even though only 80-90% of the free-carrier concentration was restored at this annealing temperature. These data indicate that the shallow acceptor level observed in NTD silicon has little if any effect on the MCL as observed by PCD.

OPTICAL PROPERTIES STUDIES OF NEUTRON-TRANSMUTATION-DOPED SILICON

R. T. Young R. F. Wood
J. W. Cleland P. H. Fleming

The infrared (IR) absorption spectra of NTD silicon is strongly dependent on the fast-neutron fluence to which the sample has been exposed. Figure 2.34, which is a graph of IR transmission vs wavelength, shows three features. First, the absorption is so strong in the short wavelength ($\leq 3\ \mu m$) region that the more heavily irradiated samples (see Table 2.4) are nearly opaque with absorption coefficients $\geq 50\ cm^{-1}$. The result that the observed transmission cutoff point shifts to longer wavelengths with increasing fast-neutron fluence will be referred to as "band-gap narrowing." Second, the near-edge absorption extending from the fundamental band edge to longer wavelengths is clearly visible. Third, the 1.8-μm band associated with divacancies is not observed in more heavily irradiated silicon because of band-gap narrowing and near-edge absorption.

No irradiation-induced IR active centers were observed in the intermediate wavelength range (5-15 μm) for a fast-neutron fluence up to 10^{20} neutrons/cm^2. Single-phonon bands were observed at 488, 410, and 322 cm^{-1}, with two additional weak bands at 545 and 525 cm^{-1} in the longer wavelength (15-50 μm) range, in measurements at both room and liquid-nitrogen temperature. Table 2.4 lists the absorption coefficients of the near-edge, divacancy (1.8 μm), and single-phonon (20.5 μm) absorptions

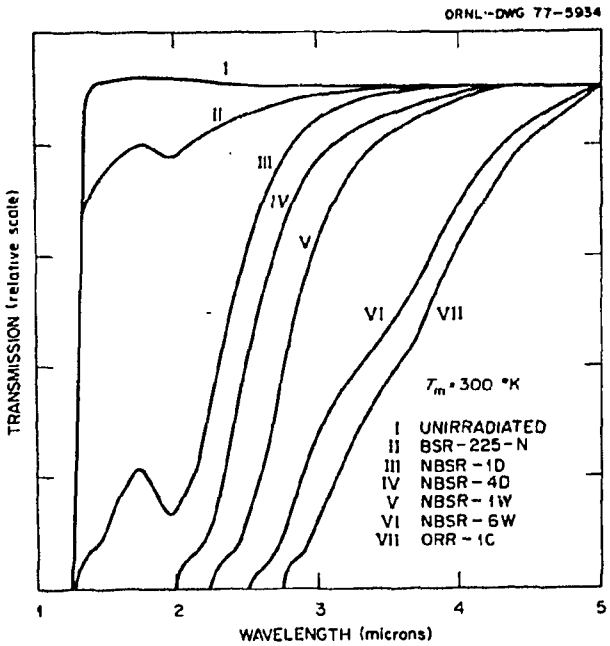

Fig. 2.34. The infrared transmission spectra of unirradiated silicon (I) and of silicon irradiated to different fast-neutron fluences (II-VII) as listed in Table 2.4.

Table 2.4. Production of infrared active centers in NTD silicon

Sample	NTD phosphorus concentration (cm^{-3})	Fast neutron fluence, neutrons/cm^2 (>1 MeV)	Absorption coefficient (cm^{-1})			Divacancy production rate (cm^{-1})
			1.8 μm	3.0 μm	20.5 μm	
BSR-225-N	2.0×10^{14}	5.0×10^{15}	0.096	[a]	[a]	1.54
BSR-1-CP15	2.0×10^{13}	3.4×10^{16}	0.610	0.15	[a]	1.44
BSR-5-CP15	1.1×10^{14}	1.9×10^{17}	3.67	0.34	0.15	1.55
BSR-10-CP15	1.4×10^{14}	2.4×10^{17}	4.70	0.42	0.20	1.57
NBSR-1D	1.8×10^{15}	1.2×10^{18}	10.8	0.81	0.49	0.72
NBSR-4D	6.7×10^{15}	4.8×10^{18}	5.3	1.34	0.96	0.29
NBSR-1W	1.0×10^{16}	8.4×10^{18}	4.1	2.45	1.15	0.15
NBSR-3W	3.0×10^{16}	2.5×10^{19}	2.1	4.76	2.85	0.02
NBSR-6W	6.0×10^{16}	5.0×10^{19}	[a]	6.80	3.74	[a]
ORR-1C	5.0×10^{16}	1.0×10^{20}	[a]	14.20	9.36	[a]

[a] Not observable.

for various samples. These data indicate that the absorption coefficients of the near-edge and single-phonon absorptions increase with fast-neutron fluence in a similar manner while the divacancy absorption saturates with fast-neutron fluence at about 10^{18} neutrons/cm^2.

Isochronal annealing results for the near-edge and divacancy absorption are shown in Fig. 2.35. These data indicate that both anneal in a similar manner for samples irradiated to a moderate ($\leqslant 5 \times 10^{18}$ neutrons/cm^2) fast-neutron fluence. However, the annealing of the near-edge absorption covers a broad temperature range for more heavily irradiated samples. The observed dependence of the annealing behavior on fast-neutron fluence suggests a complex annealing mechanism. Since the divacancy production rate as shown in Table 2.4 indicates that the divacancy is one of the dominant types of defects in silicon irradiated up to a fast-neutron fluence of about 10^{18} neutrons/cm^2, it is reasonable to attribute the annealing stage at 250°C to divacancy annihilation at lattice sinks, as suggested by Cheng and Lori.[1]

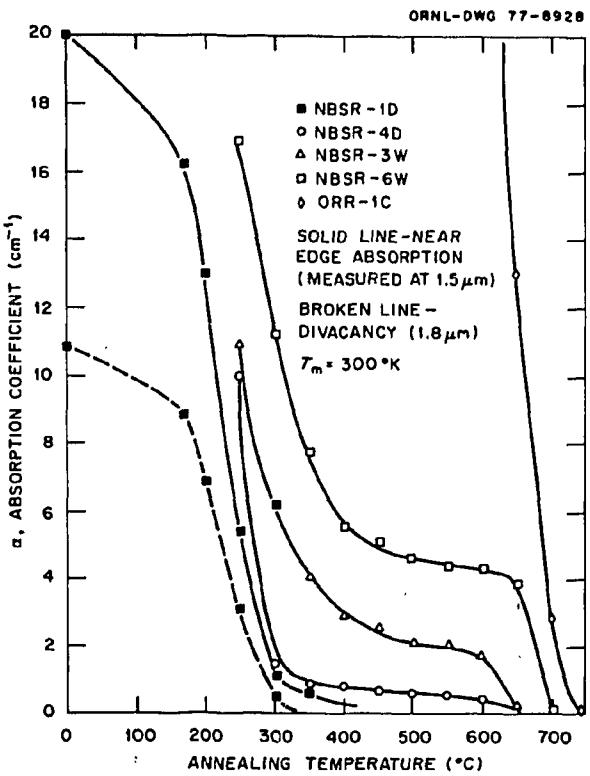

Fig. 2.35. Absorption coefficients of the near-edge and divacancy absorption as a function of isochronal annealing temperatures for silicon samples irradiated to different fast-neutron fluences as listed in Table 2.4.

The broad annealing range in more heavily irradiated silicon can then be attributed to the breakup of defect clusters. The annealing of the near-edge absorption was closely related to the recovery of electron mobility, which further confirms our postulate that defect clusters are responsible for the near-edge absorption.

---

1. L. J. Cheng and J. Lori, *Phys. Rev.* 171, 856 (1968).

ELECTRICAL PROPERTIES STUDIES OF NEUTRON-TRANSMUTATION-DOPED POLYCRYSTALLINE SILICON

R. T. Young J. W. Cleland R. F. Wood

The use of polycrystalline silicon (polysil) in the fabrication of photovoltaic devices is under widespread investigation; however, a better understanding of the effects of grain boundaries on electrical properties is needed. Seto[1] used ion implantation followed by annealing to obtain a uniform dopant distribution in the grains of thin film polysil samples. He demonstrated that grain boundaries act to decrease the majority carrier mobility until the dopant concentration exceeds that required to saturate the electronic states associated with the grain boundaries. We have used transmutation doping to introduce uniform phosphorus concentrations of accurately known magnitudes into thick polysil samples. The van der Pauw technique was used to determine the free-carrier concentration and mobility after annealing at 750°C for 1 hr to remove the radiation damage. Figure 2.36, which is a graph of the carrier mobility vs carrier concentration, indicates that the carrier mobility as a function of dopant concentration decreases to a pronounced minimum at about 10^{15} phosphorus atoms per cm^3 and then increases with increasing dopant concentration. These data were obtained on chemical vapor deposited (CVD) polysil samples with an average grain size of about 25 μm, estimated from electron microscopy. Similar measurements on single-pass float-zone refined polysil samples of much larger grain size show that the mobility minimum occurs at a lower total dopant concentration. These data are consistent with Seto's model of free-carrier trapping at the grain boundaries; they are not consistent with Fripp's model[2] of dopant migration to grain boundaries during CVD or during high-temperature annealing. One can use Seto's model to estimate from

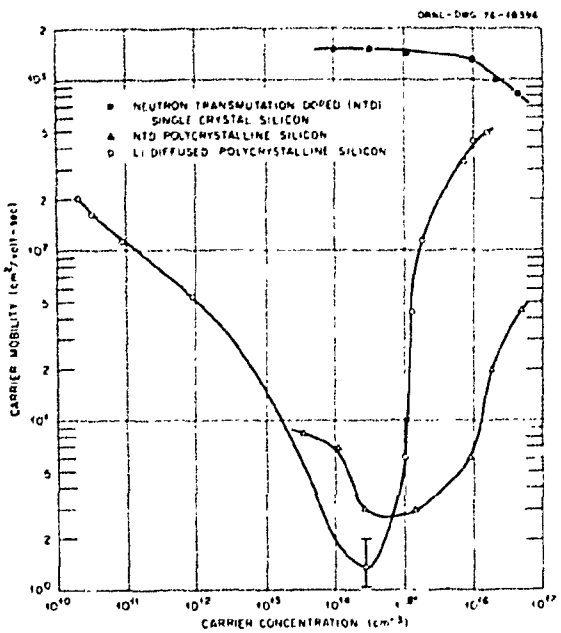

Fig. 2.36. Carrier mobility vs carrier concentration for NTD and lithium-diffused silicon.

the position of the mobility minimum in our CVD polysil that the average grain size is 33 μm, which is in good agreement with the estimate of about 25 μm from electron microscopy.

We have also diffused lithium from a paint-on source into single crystal silicon and polysil samples. The lithium diffusion rate in polysil is one or two orders of magnitude greater than in a single crystal silicon because of the high grain boundary mobility. The lithium-diffused polysil shows a mobility minimum at a measured carrier concentration of about 10^{15} cm^{-3} as indicated in Fig. 2.36. Moreover, the carrier mobility of the lithium-diffused polysil is more than an order of magnitude greater than that of the NTD polysil at an equivalent carrier concentration of about 10^{16} cm^{-3}. This suggests that the grain boundary effect in polysil can be diminished by an inward diffusion of lithium along grain boundaries. However, rapid out-diffusion at temperatures $\leq$400°C was also observed, and this may prohibit the use of lithium diffusion to diminish grain boundary effects in polysil, if any subsequent high-temperature treatment is required.

1. J. W. Y. Seto, *J. Appl. Phys.* 46, 5247 (1975).
2. A. L. Fripp, *J. Appl. Phys.* 46, 1240 (1975).

DISORDERED REGION MODEL FOR FAST-NEUTRON-IRRADIATED SILICON

R. T. Young J. W. Cleland

Room temperature electrical property measurements of single crystal silicon irradiated with a large fast-neutron fluence indicate that before annealing, the material is essentially intrinsic and that the electron mobility is comparable to that of polysil with an average grain size of 50-100 μm. This implies the existence of highly disordered regions. Although the fast-neutron-induced lattice defect structure is different from the grain boundary structure of polysil, the argument required to explain the low mobility is similar in both materials in that disordered regions act as barriers to the movement of majority carriers. One can use the defect cluster model of Gossick[1] and Crawford and Cleland[2] to illustrate schematically the potential energy in the disordered region and the surrounding space-charge region as shown in Fig. 2.37. The average radius of a defect cluster in a silicon sample irradiated with a fast-neutron fluence of about 10^{20} neutrons/cm^2 was $r_1 \sim 10$ Å, and the local defect concentration was estimated to be about 5×10^{19} cm^{-3} (ref. 3). The corresponding potential barrier height from the defect-cluster model is $\psi_p = 0.48$ eV, and the radius of the space-charge region is $r_2 = 100$ Å. Even by assuming one defect cluster for every ten scattered neutrons (which may be an underestimate), the space-charge regions still overlap extensively. The retention

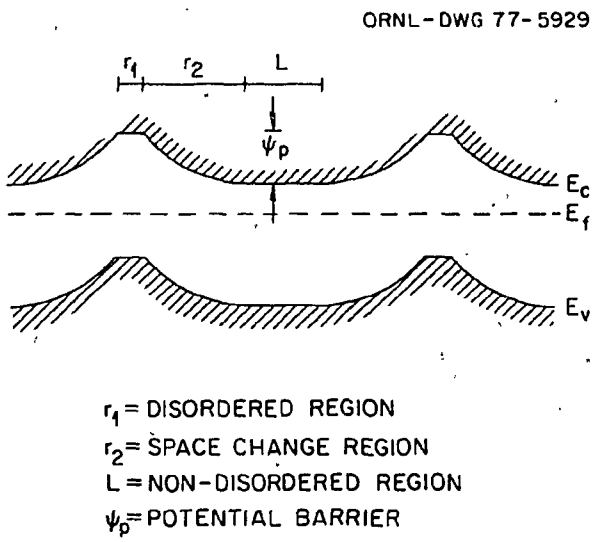

Fig. 2.37. The potential distribution of the conduction band and valence band in the vicinity of the disordered region.

of essentially intrinsic behavior and extremely low mobility to an annealing temperature of 600-650°C indicates that the defect clusters are stable to high temperatures, a fact that is also confirmed by x-ray diffuse scattering experiments reported elsewhere in this annual report.[4]

It is also interesting to point out that an annealing temperature of at least 700-750°C is required for ion-implanted silicon. The vacancy/interstitial associated defect and/or simple complexes can be annealed below about 600°C, but large clusters and/or disordered regions such as dislocation loops or stacking faults begin to be detected above about 600°C. In general, it seems evident that the annealing of lattice damage in neutron-irradiated or ion-implanted silicon exhibits similar features. This is not surprising because the average energy transmitted when a fast neutron collides with a lattice atom is 30 to 100 keV, and the recoiling lattice atom will produce lattice defects along its track similar to those produced by a 20- to 100-keV ion implant.

1. B. R. Gossick, *J. Appl. Phys.* 30, 1214 (1959).
2. J. H. Crawford, Jr., and J. W. Cleland, *J. Appl. Phys.* 30, 1204 (1959).
3. B. C. Larson, unpublished data.
4. Bennett C. Larson, R. T. Young, and F. A. Sherrill, "X-Ray Study of Defect Clusters in Neutron-Transmutation-Doped Silicon," this report.

STRUCTURAL DEFECTS IN POLYCRYSTALLINE SILICON AND THEIR EFFECT ON SOLAR CELL EFFICIENCY[1]

J. Narayan

Although extensive electron microscope studies of defect structures in silicon single crystals have been made, it appears that little or no attention has been given to the defect structures in polysil because it has been used almost exclusively as a source material subjected to further purification and growth into device-grade single crystals. There is current interest in polysil for fabrication of less expensive solar cells; however, improvement in the electrical properties will be necessary in order to achieve reasonable solar cell efficiency. Because most structural defects degrade the electrical properties of both *p*- and *n*-type silicon, the characterization of their structures will provide a basis for selection of better material and/or processes for reducing defect densities. The present work is part of a program which includes the evaluation and development of polysil as a solar cell material. The observations reported here were made on polysil obtained from Texas Instruments and Monsanto and are believed to be more or less representative of the structures observed in other polysil material.

Figure 2.38 shows examples of small-angle boundaries in which the characterization of the dislocation structure in the boundaries could be made. Figure 2.38*a* shows a small-angle tilt boundary that consists of edge dislocations with $a/2[101]$ Burgers vectors. An example of a twist boundary, which consists of $a/2[01\bar{1}]$ and $a/2[101]$, is shown in Fig. 2.38*b*. At the nodes, which are denoted as *n* in Fig. 2.38*b*, $a/2[01\bar{1}]$ and $a/2[101]$ Burgers vectors react to give $a/2[110]$ Burgers vectors. A tilt boundary in Fig. 2.38*c* consisting of one set of $a/2[101]$ edge dislocations changes into a mixed boundary by acquiring another set of $a/2[110]$ dislocations of near screw orientation. Boundaries of mixed character which undergo changes of the type seen in Fig. 2.38*c* are more frequent than the simple tilt and twist boundaries shown in Figs. 2.38*a* and 2.38*b*. In addition to the boundary structures, this material contains a relatively high density of dislocations, and stacking faults having $a/6\langle 112\rangle$ and $1/3\langle 111\rangle$ Burgers vectors have been identified.

It is expected that most of the defect structures observed in the polysil will adversely affect its electrical properties. First, the direct trapping of impurities (dopants) as a result of the elastic interaction between the impurities and dislocations will lead to impurity segregation[2] and consequently nonuniform electrical properties. Edge-type dislocations and the partial edge dislocations bounding stacking faults are more detrimental than screw-type dislocations. In addition to segregation, the incomplete atomic bonding at the cores of the dislocations results in the formation of trapping states which lead to trapping and recombination of free carriers.[3,4] Improvement in the electrical properties of polysil is expected to be obtained by reduction of the defect density of all types and by the elimination of boundaries that are not normal to the *p-n* junction of the solar cell.

1. Summary of paper: p. 296 in *Proceedings of the Thirty-fifth Annual Meeting of the Electron Microscopy Society of America*, ed. by G. W. Bailey, Claitor's Press, Baton Rouge, La., 1977.
2. M. E. Cowher and T. O. Sedgwick, *J. Electrochem. Soc.* 119, 1565 (1972).
3. J. R. Patel, L. R. Tastardi, and P. E. Freeland, *Phys. Rev. B* 13, 3548 (1976).
4. R. Labusch and W. Schröter, p. 56 in *Lattice Defects in Semiconductors*, The Institute of Physics, London, 1975.

PHOTO 3506-77

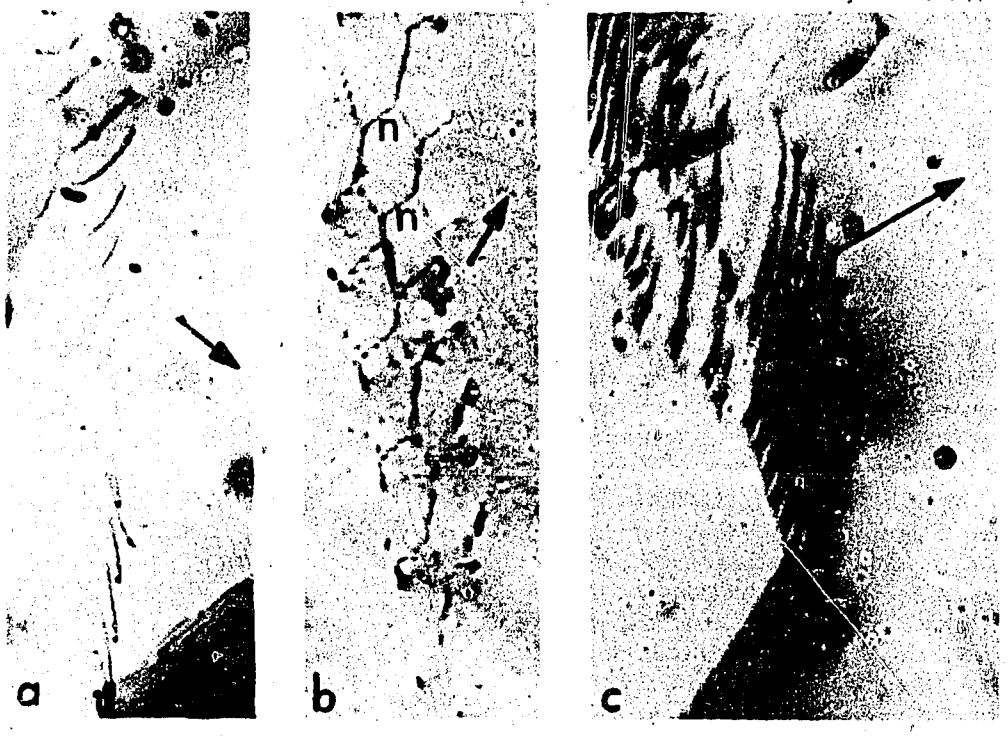

Fig. 2.38. Electron micrographs showing (*a*) pure tilt subboundary, (*b*) pure twist subboundary, and (*c*) mixed subboundary. The arrows indicate the directions of diffraction vectors [331], [220], and [311], respectively, and their length is 0.3 μ.

X-RAY STUDY OF DEFECT CLUSTERS IN NEUTRON-TRANSMUTATION-DOPED SILICON

Bennett C. Larson R. T. Young
F. A. Sherrill

Integral x-ray diffuse scattering has been used to study neutron-irradiation-induced clusters in NTD silicon and to study the postirradiation annealing characteristics of these clusters. Bulk crystals irradiated in the ORR to obtain NTD phosphorus doping levels of 5×10^{16} cm^{-3} received concomitantly a fast-neutron dose of about 10^{20} cm^{-3}. These crystals were investigated with CuKα x rays using the diffuse scattering near the 333 Bragg reflection. The diffuse scattering was measured after irradiation and after 30-min isochronal anneals to 550, 650, and 700°C in which it was found that rather large numbers of small defect clusters were formed. These clusters, presumably small dislocation loops, were found to have characteristic sizes of about 9 Å before annealing and, while decreasing in number, were found to increase in size to 11, 13, and 28 Å after the three annealing treatments. The fraction of the original number of point defects (present in the form of loops) retained after the heat treatments of 550, 650, and 700°C was found to be 0.5, 0.2, and 0.01 respectively.

These results can be correlated with the optical and electrical measurements of IR near-edge absorption, electron mobility, and free-carrier concentration, which also show strong recovery in the temperature range of 600–700° C. Initial x-ray results on NTD silicon irradiated in a reactor environment (NBSR) with a higher thermal- to fast-neutron ratio have indicated smaller cluster sizes and substantial defect annealing at lower temperatures that can be correlated with earlier recovery seen in the optical and electrical properties as well.

ELECTRON PARAMAGNETIC RESONANCE STUDIES OF NEUTRON-TRANSMUTATION-DOPED SILICON

M. M. Abraham R. T. Young

The EPR spectrum of neutron-irradiated single crystal silicon exhibits many anisotropic radiation damage lines. Figure 2.39 shows the spectra obtained from a sample irradiated with a fast-neutron ($\geq$1 MeV) fluence of 2.5×10^{19} neutrons/cm^2 (*a*) after annealing at 550°C for 20 min and (*b*) after a subsequent anneal at 650°C for 20 min. It is evident that not only is the radiation damage essentially removed in (*b*) but also that the main neutron-transmutation-induced phophorus lines appear at different field positions from those for the radiation damage lines. Figure 2.40 shows similar spectra obtained from a sample irradiated with a fast-neutron fluence of about 10^{20} neutrons/cm^2 after an identical annealing schedule. The microwave power level was reduced for the second sample, but saturation effects can be seen in both sets of data. No attempt was made to orient the samples relative to the magnetic field. Since a higher temperature anneal is required for the second sample, it appears that the annealing of the radiation damage for the two samples is dependent on the fast-neutron fluence. In any event, annealing at 750°C for 20–30 min removes any paramagnetic species, which is in agreement with electrical and optical property results as described in other subsections of this annual report.[1,2]

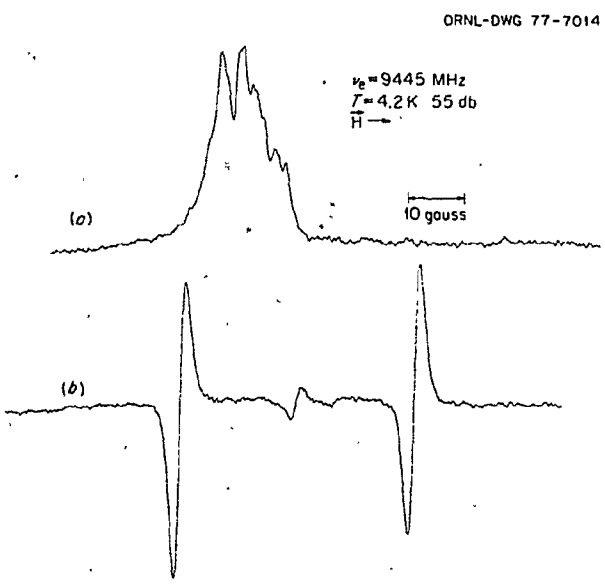

Fig. 2.39. EPR spectra of NTD silicon after a three-week irradiation (fast-neutron fluence about 2.5×10^{19} neutrons/cm^2) in the National Bureau of Standards Reactor and subsequent annealing. (*a*) 550°C for 20 min. (*b*) 650°C for 20 min.

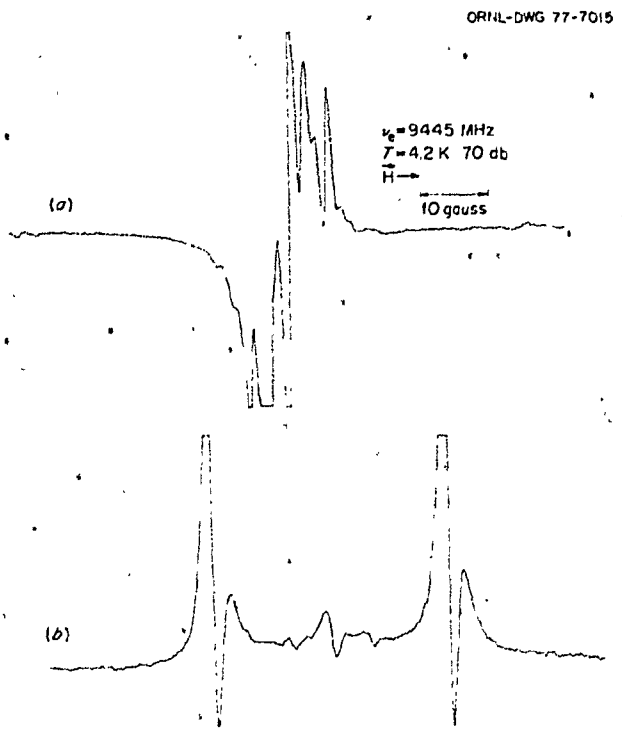

Fig. 2.40. EPR spectra of NTD silicon after an 11-day irradiation in the ORR (fast-neutron fluence about 10^{20} neutrons/cm^2) and subsequent annealing. (*a*) 650°C for 20 min. (*b*) 750°C for 20 min.

1. R. T. Young, J. W. Cleland, and R. F. Wood, "Electrical Properties Studies of Neutron-Transmutation-Doped Silicon," this report.
2. R. T. Young et al., "Optical Properties Studies of Neutron-Transmutation-Doped Silicon," this report.

REACTOR IRRADIATION FACILITIES FOR NEUTRON TRANSMUTATION DOPING OF SILICON

J. W. Cleland C. C. Robinson

A new thermal neutron facility (D_2O tank), shown schematically in Fig. 2.41, has been constructed and will be installed in the pool of the BSR at ORNL. The new tank will accommodate ingots or wafers up to 6 in. in diameter and will have provisions for raising,

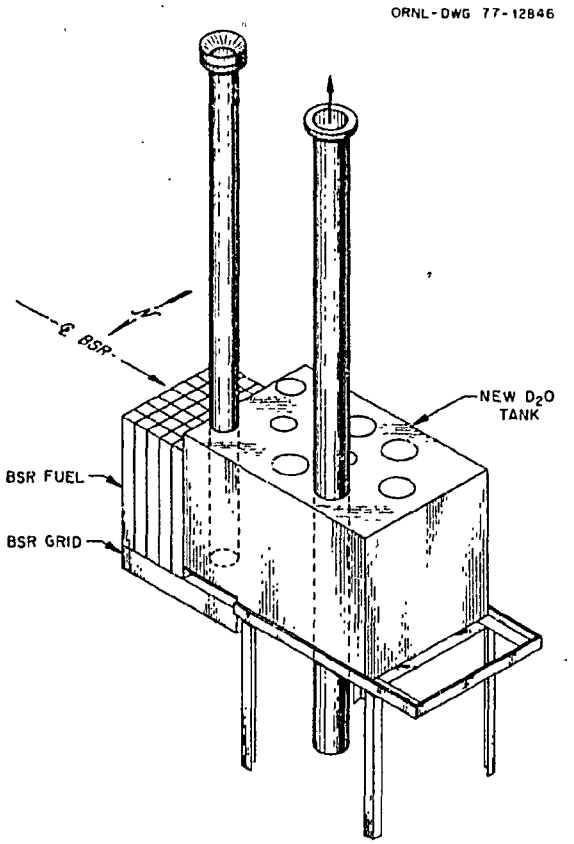

Fig. 2.41. New thermal neutron facility (D_2O tank) to be installed in the Bulk Shielding Reactor.

lowering, and rotating the samples to maximize the axial and radial dopant uniformity. Another feature of the tank is that the sample tubes terminate 8 ft above the tank in a flange or funnel arrangement; this will permit sample exchange under water without the use of "*S*" shaped irradiation tubes. Any of the tubes, except those immediately adjacent to the BSR core, can be either converted to "*S*" shape for dry irradiations or plugged with graphite, magnesium, or D_2O-filled cylinders to achieve maximum thermal neutron flux and thermal- to fast-neutron ratio in the other irradiation positions.

One of the slant Engineering Facility (EF-2) irradiation tubes outside the permanent beryllium core of the High Flux Isotope Reactor (HFIR) was used for a test irradiation of single crystal silicon and polysil ingot sections. The samples were held in slots in an aluminum plate with aluminum wire, and the plate was centered inside a cylindrical aluminum container with spacers on the outside to ensure an even flow of cooling water. The entire assembly was rotated 180° after one-half of the reactor duty cycle to minimize the effect of the neutron flux gradient. Approximately 3×10^{16} phosphorus atoms per cm^3 were introduced in the silicon as a consequence of an irradiation of one duty cycle (23 days). Another test irradiation is being considered in one of the vertical experimental facilities (RB 1, 3, 5, or 7) in the permanent beryllium core of the HFIR to introduce at least 10^{17} phosphorus atoms per cm^3 in both single and polysil ingot sections.

SOLAR CELL FABRICATION

R. D. Westbrook P. H. Fleming
B. F. Early T. L. Polgreen
R. A. Todd[1]

The effort in solar cell fabrication has been directed towards achieving a well-behaved, reproducible process rather than one to attain the maximum efficiency, because we are primarily interested in comparative measurements between NTD and conventionally doped silicon solar cells. The question of ultimate efficiency can best be answered by those highly specialized manufacturers capable of making so-called "state-of-the-art" devices.

Our cells are made in a sequence of about 12 operations involving cutting, polishing and/or etching, diffusion or ion implant, cleaning, metallizing, etc. While disaster lurks at every step, the two key processes are diffusion (or ion implant) and contact metallization. We diffuse boron in through the front face of the cell to a depth of 3000–4000 Å, resulting in the desired p^+-n structure. We have not yet set up a procedure for measuring diffusion depth (there are several), so we base the diffusion time and temperature schedule on published information and monitor the results with sheet resistance measurements on the diffused layer. Electrical contact must be made to both faces. The back face is simply covered with an aluminum or nickel layer which requires a relatively simple procedure. The front contact, however, is necessarily made in the form of an opaque metallized grid pattern in order to satisfy the requirements of very low series resistance through the cell. In high-performance cells, there is a very fine trade-off between the series resistance and the net active front area of the device not covered by the metallized grid. We also have looked at silk-screen processes for the front contact because they offer advantages in time, simplicity, and capital investment. Other investigators are also exploring

screen-printed contacts. Currently, however, we seem to get somewhat more consistent results with the evaporated metal process.

---

1. Instrumentation and Controls Division, ORNL.

NEUTRON-TRANSMUTATION-DOPED SILICON SOLAR CELLS

R. D. Westbrook T. L. Polgreen
J. W. Cleland R. F. Wood
P. H. Fleming R. T. Young

We have now fabricated hundreds of test solar cells using conventional and NTD silicon and covering phosphorus doping concentrations from about 10^{14} to 10^{17} cm^{-3} in both single crystal silicon and polysil. We are searching primarily for any statistically significant difference between the two types of doping processes in terms of conversion efficiency, and to date, we have found none. If this result is confirmed by further testing, then we have demonstrated that the requirement for areal and spatial homogeneity of the primary dopant for p^+-on-n solar cells is adequately met by conventionally doped silicon, at least under one-sun conditions. In the immediate future, we need to verify these results using solar cells made with our recently acquired industrial-standard diffusion equipment. We also need to compare conventionally doped and NTD single crystal silicon and polysil under high-level concentration conditions (50 to 100 suns) where areal and spatial homogeneities may be of more importance than they appear to be without concentration.

FRACTURE

"IN SITU" OBSERVATION OF CRACK PROPAGATION BY TRANSMISSION ELECTRON MICROSCOPY

J. Narayan S. M. Ohr

Problems of crack nucleation and propagation associated with fracture in solids have been the subject of numerous experimental and theoretical investigations in the past, but the basic mechanism of the phenomena is not well understood at present. We have initiated a program to study the fundamental aspects of fracture in which the physical processes occurring at the crack tip will be examined on a microscopic scale by transmission electron microscopy. As an initial approach to the problem, we have observed the propagation of cracks during "in situ" tensile deformation of ductile as well as brittle solids in an electron microscope.

Figure 2.42 shows a micrograph taken from a single crystal sample of type 316 stainless steel representing ductile solids. As the stress was applied to the crystal, a crack was initiated at the edge of the hole on the right. From the crystallographic analysis, the fracture plane is identified as $(\bar{1}11)$. The most noticeable feature is the band ahead of the crack tip with intense plastic activity. The dislocation density is extremely high near the crack tip, and it decreases gradually away from the tip. The band is made up of dislocations lying in the $(\bar{1}11)$ plane which would have Burgers vectors $a/2[\bar{1}01]$ and/or $a/2[0\bar{1}1]$. Evidence of plastic activities on the other two slip planes, namely on $(11\bar{1})$ and $(1\bar{1}1)$, can be seen as narrow slip bands running obliquely into the crack plane.

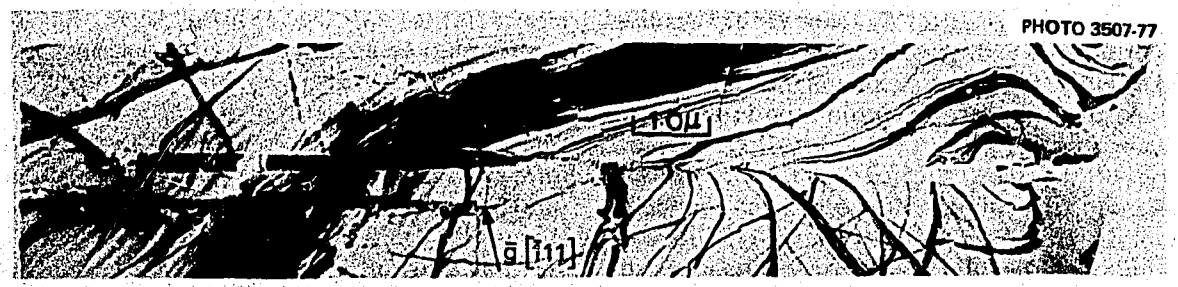

Fig. 2.42. Dislocation structure around a propagating crack in type 316 stainless steel single crystal sample. The sample was deformed in the electron microscope in pure tension.

Figure 2.43 shows a similar observation made in a single crystal of MgO representing brittle materials. The crack plane is identified as the (100) plane, and it runs along the [010] direction. The dislocations observed in the vicinity of the crack are in contrast under the (200) reflection. These dislocations were in contrast under the (220) and ($2\bar{2}0$) reflections but were out of contrast under the (020) reflection. From this contrast behavior, the Burgers vectors of these dislocations were deduced to be $a/2[101]$ and $a/2[10\bar{1}]$. From the stereomicroscopy and other geometric considerations it appears that the dislocations on one side of the crack represented the $[101]/(\bar{1}0\bar{1})$ slip system while those on the other side the $[10\bar{1}]/(101)$ slip system.

These observations are rather preliminary; hence it is too early to draw any definite conclusions regarding the nature of the distribution of dislocations around the crack tip. However, the crystallographic information contained in these micrographs appears to agree with the predictions of the theory of the formation of plastic zones around a crack. According to Dugdale,[1] the plastic zones under uniaxial tensile loading in plane stress should extend out on two 45° planes which bisect the angle between the tensile axis and the leading edge of the crack and which are parallel to the direction of crack propagation. This type of behavior was observed by Hahn and Rosenfield[2] in their sheet tensile samples by the etch-pits technique. The present observations represent the electron microscope evidence for the formation of plastic zones near a crack similar to those expected from theory and thus render support for the validity of thin foil electron microscope techniques.

1. D. S. Dugdale, *J. Mech. Phys. Solids* 8, 100 (1960).
2. G. T. Hahn and A. R. Rosenfield, *Acta Metall.* 13, 293 (1965).

FORCES ON DEFECTS IN LINEAR ELASTICITY

S.-J. Chang[1] S. M. Ohr

The energy momentum tensor in elasticity was introduced by Eshelby[2] to calculate the change of energy for an elastic medium containing defects. The crack extension force is defined as the change of energy per unit extension of the crack. Therefore the energy momentum tensor can be used to represent the crack extension force. Leibfried's[3] recent definition of the energy momentum tensor differs from that of Eshelby in that the effect of body force can be included. Since plastic deformation, or a distribution of dislocations, can be represented by the equivalent body forces, we will use this tensor quantity to calculate the effect of the distribution of dislocations on the crack extension force.

Let l be the energy density of the elastic body given by

$$l = \frac{1}{2} C_{iknn} \frac{\partial u_i}{\partial u_k} \frac{\partial u_m}{\partial x_n} - u_i f_i \ ,$$

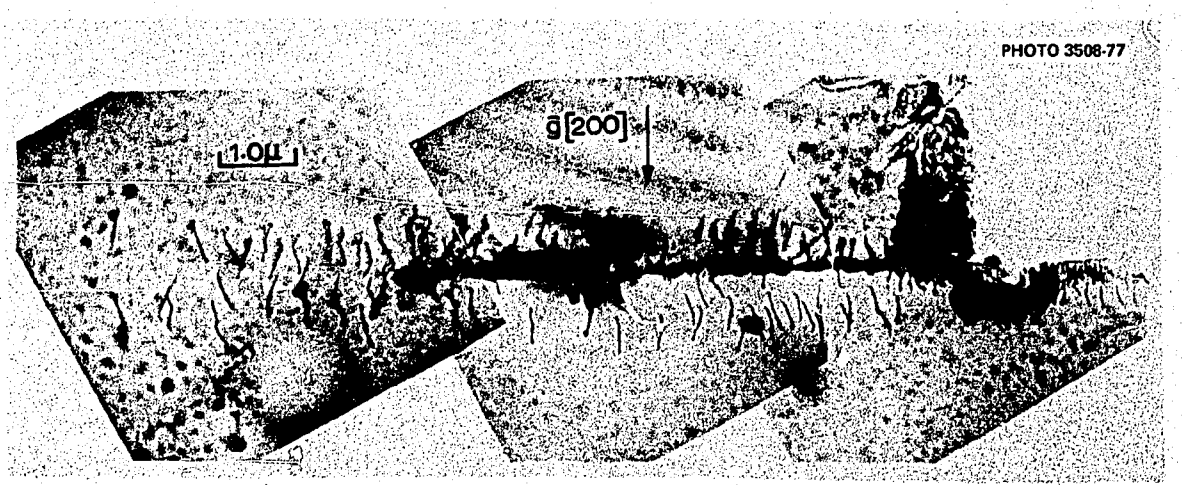

Fig. 2.43. Dislocation structure around a crack in an MgO single crystal. The dislocations are associated with the 45° shear-type plastic zones of the $[101]/(10\bar{1})$ slip systems.

where f_i is the body force, u_i is the displacement vector, and C_{ikmn} are the elastic constants. By differentiating with respect to x_m, we have

$$\frac{\partial I(u_i, u_{i,k}, x_i)}{\partial x_m} = \frac{\partial I}{\partial u_i}\frac{\partial u_i}{\partial x_m} + \frac{\partial I}{\partial u_{i,k}}\frac{\partial u_{i,k}}{\partial x_m} + \frac{\partial \hat{I}}{\partial x_m} ,$$

where

$$u_{i,k} = \frac{\partial u_i}{\partial x_k}$$

and $\partial \hat{I}/\partial x_m$ is the explicit derivative of I; that is,

$$\frac{\partial \hat{I}}{\partial x_m} = -u_i \frac{\partial f_i}{\partial x_m} .$$

It can be shown that

$$\frac{\partial \hat{I}}{\partial x_m} = \frac{\partial \mathit{II}_{mk}}{\partial x_k} = -u_i \frac{\partial f_i}{\partial x_m} ,$$

where II_{mk}, defined by

$$\mathit{II}_{mk} = I\delta_{mk} - \sigma_{ik}u_{i,m} ,$$

is the momentum tensor of Leibfried and σ_{ik} is the stress tensor. The momentum tensor of Eshelby is

$$e_{mk} = e\delta_{mk} - \sigma_{ik}u_{i,m} ,$$

where e is the strain energy density. The crack extension force can be shown to be

$$F_m = \int_V \frac{\partial \mathit{II}_{mk}}{\partial x_k}\, dv ,$$

where V is a volume enclosing the crack edge.

Suppose that internal stress is present in the elastic body due to the presence of defects. Let $\epsilon'_{ij}(x_i)$ be the corresponding self-strain that is considered to be the source of the internal stress. The total strain

$$\epsilon'_{ij} = \epsilon'_{ij} + \epsilon_{ij}$$

is defined to be the sum of the self-strain and the elastic strain. It can be shown that a fictitious body force

$$f'_i = -\frac{\partial}{\partial x_e}(C_{ikmn}\epsilon'_{mn})$$

can be used to replace the effect of the internal stress. This body force can be introduced into the expression for II_{mk} to calculate the effect of the presence of defects on the crack extension force. This provides a method of introducing defect structures into fracture mechanics, and further development of this approach is expected to lead to a theoretical basis for dealing with the microscopic structural aspects of crack propagation.

---

1. Computer Sciences Division, UCC-ND.
2. J. D. Eshelby, p. 77 in *Inelastic Behavior of Solids*, ed. by M. Kanninen, McGraw-Hill, New York, 1970.
3. G. Leibfried, private communication.